Coupling cell shape and velocity leads to oscillation and circling in keratocyte galvanotaxis

Ifunanya Nwogbaga¹ and Brian A. Camley^{1,2}
¹Department of Biophysics and ²Department of Physics & Astronomy,
Johns Hopkins University, Baltimore, Maryland

During wound healing, fish keratocyte cells undergo galvanotaxis where they follow a woundinduced electric field. In addition to their stereotypical persistent motion, keratocytes can develop circular motion without a field or oscillate while crawling in the field direction. We developed a coarse-grained phenomenological model that captures these keratocyte behaviors. We fit this model to experimental data on keratocyte response to an electric field being turned on. A critical element of our model is a tendency for cells to turn toward their long axis, arising from a coupling between cell shape and velocity, which gives rise to oscillatory and circular motion. Galvanotaxis is influenced not only by the field-dependent responses, but also cell speed and cell shape relaxation rate. When the cell reacts to an electric field being turned on, our model predicts that stiff, slow cells react slowly but follow the signal reliably. Cells that polarize and align to the field at a faster rate react more quickly and follow the signal more reliably. When cells are exposed to a field that switches direction rapidly, cells follow the average of field directions, while if the field is switched more slowly, cells follow a "staircase" pattern. Our study indicated that a simple phenomenological model coupling cell speed and shape is sufficient to reproduce a broad variety of different keratocyte behaviors, ranging from circling to oscillation to galvanotactic response, by only varying a few parameters. Significance: Many cells follow electric fields - "galvanotaxis" - using this cue to heal wounds. How can cells respond to electric fields that change rapidly? What controls what type of pattern cells crawl in? We model and predict the migration patterns of a keratocyte (a cell derived from a fish scale), both with and without an electric field present. The key element of our model is that a cell's shape is coupled to its velocity. Our model reproduces cell crawling patterns like persistent motion, oscillatory motion about a field, and circular crawling, and quantitatively recapitulates the cell's directionality after an electric field is turned on. We make predictions about how cell shape, speed, and stiffness affect cell motility.

I. INTRODUCTION

Directed cell migration is necessary for processes like wound healing, immune response, and developmental biology [1]. Epidermal keratocyte cells in fish and amphibians can follow electrical fields to heal wounds [2-4]. It has been known since the 19th century that skin wounds generate electric fields [5, 6]. In vivo, injuries disrupt the transepithelial potential [7, 8], short-circuiting the injured section, and leading to a potential difference between the injured section and healthy tissue, creating an endogenous electric field that guides migration of cells towards the wound [6, 9]. These fields are generally steady in time (DC fields) [6, 10]. In vitro, many single cells also have strong directional response to electric fields. Dictyostelium discoideum, human mesenchymal stem cells, fibroblasts, and keratocytes in electric fields typically migrate towards the cathode [8, 11–15]. Keratocytes in particular are relatively geometrically simple and have become a useful model system for cell motility in response to electric fields [16–19]. Field strengths as low as 0.25 V/cm are enough to induce single and collective cell migration in keratocytes [20], though other cell types like neural crests exhibit galvanotaxis in fields as weak as 0.1 V/cm [21]. These fields are too weak to physically drag cells – the cells sense and respond to the field using their motility machinery [20]. Interestingly, in addition to their typical persistent motion, keratocytes also

display spontaneous circular motion, a persistent turning driven by asymmetries in traction forces and myosin contractility at the rear of the cell [16, 18, 19]. This behavior is also seen in detailed molecular models resolving cell shape and polarity [16–18, 22, 23] and emerges from self-propelled deformable particle models [24]. In the presence of a field, keratocytes may oscillate from side to side while crawling in the field direction [20].

The molecular details of galvanotaxis in keratocytes are somewhat obscure. There is evidence that galvanotaxis is driven by electrophoresis of mobile, charged membrane-attached molecules [19, 20, 25], and candidates for sensors have been identified [26–28], but the molecular-scale understanding is not as well-established as chemotaxis [1]. In addition, the details of how this spatial asymmetry on the cell surface leads to initiation of the downstream signaling cues and migration are not fully understood. Despite this uncertainty, it is clear that electric fields are a key cue in wound healing, overriding other signals [9, 29]. As the study of directed motion in electric fields is expanded to the study of groups of cells [30–36], there is a need for phenomenological models that can quantitatively describe galvanotaxis.

We developed a stochastic model of single-cell galvanotaxis describing the cell as a self-propelled deformable particle [24, 37–40], tracking the cell's shape and velocity as it follows a constant DC electric field. Shape and velocity have a natural relationship experimentally [41, 42]. This reason may contribute to why keratocytes adopt dif-

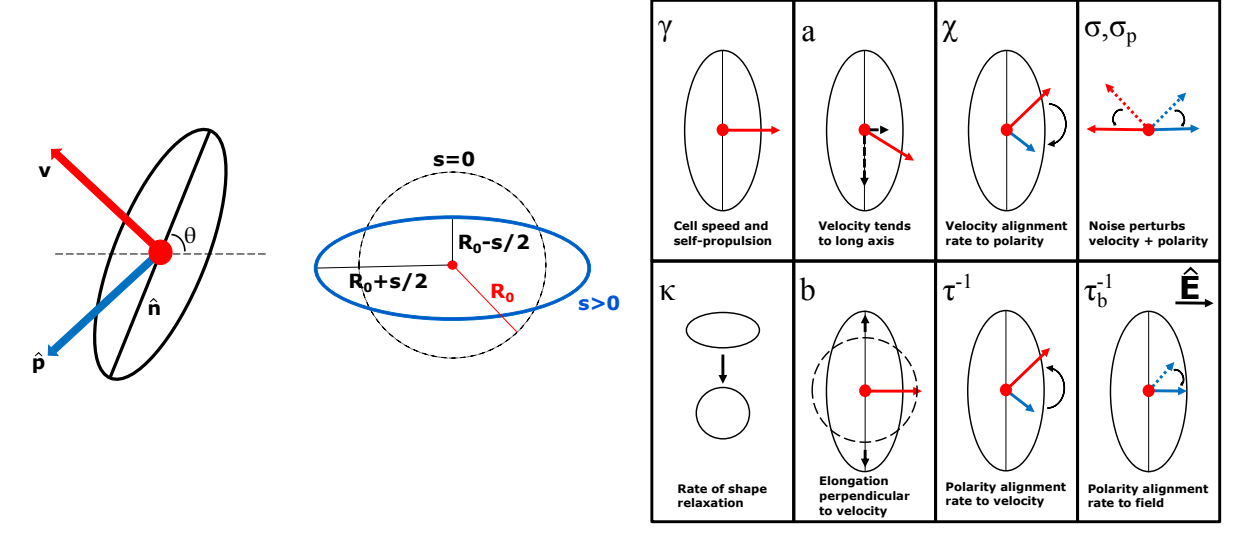


FIG. 1: Left: Cells modeled as deformable ellipses, with a velocity \mathbf{v} and an underlying biochemical polarity unit vector $\hat{\mathbf{p}}$. Their orientation is characterized by θ , the shortest angle between the cell's long axis and the $\hat{\mathbf{x}}$ -axis. The unit vector $\hat{\mathbf{n}}$ points along the cell's long axis. Cells begin as circular with radius R_0 . They can deform to ellipses with semi-major and semi-minor axes lengths of $R_0 \pm s/2$. s controls eccentricity, with s=0 denoting no deformation from a circle. Right: Schematic of the different terms in the equations of motion for velocity (Eq. 2), shape (Eq. 3), and polarity (Eq. 4).

ferent morphologies for migrating forward versus making turns [18]. To capture the effect of cell shape, we utilize the deformable self-propelled particle model of [24], as it naturally includes a coupling between the cell's velocity and its shape; this coupling is known to create circular motion. However, the model of [24] was derived as the simplest model that could describe a general selfpropelled deformable particle, including a cell, active colloid, or an emulsion droplet. Thus, we tailor this model to cell migration by introducing noise to account for random fluctuations in the intra- and extracellular environment, and a polarity angle to indicate the underlying biochemical polarization of the cell – the "compass" that responds to the electric fields. This polarity is then coupled with the cell's velocity. We show using linear stability analysis that, as in [24], this model has regimes where persistent linear crawling by the cell is stable, and others where more complex behaviors like circular motion arise. We fit this model to the data of [20] studying how keratocyte directionality responds to an activated field. We then use these parameters to show how the cell's directionality depends on features like cell speed and the rate its shape relaxes to equilibrium. Finally, we show that the cell's rate of response to a switched-on electric field also can influence its response to rapidly-switched fields, where cells may reliably follow each field direction, follow the average of the fields, or develop a more complex behavior, depending on the cell's parameters.

II. MODEL AND METHODS

Our model includes four key variables to represent the state and motion of a keratocyte: shape (characterized by a tensor $S_{\alpha\beta}$), center of mass $\mathbf{r}(t)$, velocity $\mathbf{v} = \frac{d\mathbf{r}}{dt}$, and a internal polarity direction $\hat{\mathbf{p}}$ (Fig. 1).

The symmetric traceless shape tensor $S_{\alpha\beta}$ [24] captures the extent of deformation from a circle s(t), and the orientation of the cell's long axis $\theta(t)$,

$$S_{\alpha\beta} = s \left(n_{\alpha} n_{\beta} - \frac{1}{2} \delta_{\alpha\beta} \right), \tag{1}$$

where $\delta_{\alpha\beta}$ is the Kronecker delta, n_{α} and n_{β} are the components of the unit vector $\hat{\mathbf{n}}(t) = (\cos \theta, \sin \theta)$ which points along the long axis of the cell (Fig. 1), and $\{\alpha, \beta\}$ are indices running over the coordinates $\{x, y\}$. Here, s(t) is a nonnegative number that describes the degree of deformation. s = 0 is a circular cell while increasing s increases cell eccentricity. The eigenvalues of $S_{\alpha\beta}$ are $\pm s/2$. We draw cells with a deformation s as being an ellipse with the length of the semi-major and minor axes given by $A = R_0 + s/2$ and $B = R_0 - s/2$, where R_0 is the radius the cell would have if it were circular (Fig. 1). We chose the deviation s/2 to be consistent with the definition of s in the Fourier mode representation of [39].

Our model's dynamics for $S_{\alpha\beta}$, \mathbf{v} , and $\hat{\mathbf{p}}$ are given in Eqs. 2-4 and shown schematically in Fig. 1. The cell's velocity obeys:

$$\frac{\mathrm{d}\mathbf{v}}{\mathrm{d}t} = \mu(\gamma - |\mathbf{v}|^2)\mathbf{v} - a\mathbf{\tilde{S}} \cdot \mathbf{v} - \frac{\chi}{|\mathbf{v}|}\mathbf{v} \times (\mathbf{v} \times \hat{\mathbf{p}}) + \sigma \xi(t)\hat{\mathbf{v}}_{\perp}. \tag{2}$$

The first two terms on the right hand side are from [24]. The first term describes the cell's self-propulsion, which will (in the absence of other effects) drive the cell's speed to $\sqrt{\gamma}$. γ sets the cell speed and has a natural biological basis since keratocyte cell speed is easily measurable,

with some experiments recording speeds as low as 3-15 μ m/min [42, 43], while others observed speeds up to 60 μ m/min [3, 44]. γ will then presumably be dependent on factors that regulate cell speed, e.g. the rate of actin polymerization at the leading edge and motor/clutch interactions with the substrate [45, 46]. μ was added to balance units (Appendix B). The second term on the right hand side shows how the velocity responds to cell shape: if a < 0 (which is true everywhere in the main body of this paper), velocities along the cell's major axis will increase, and velocities along the cell's minor axis will decrease, leading the velocity to tend to align to $\pm \hat{\bf n}$ (Appendix A). The tendency of \mathbf{v} to align with $\pm \hat{\mathbf{n}}$ competes with the tendency of the cell shape to expand perpendicular to the velocity (Eq. 3), leading to both circular cell motion (Fig. 2) and other complex behaviors where the long axis of the cell is not perfectly perpendicular to the velocity. There is no immediate biological analog for a; it is the coefficient of the first order term that couples \mathbf{v} and $\mathbf{\tilde{S}}$ [24]; this shape coupling may reflect Rho GT-Pase shape-sensing dynamics [17, 47], and would likely be altered by factors controlling the distribution of Rho GTPases within the cell. The third term's triple cross product (a la [48]) shows a rotation of velocity to come into alignment with the cell's polarity – i.e. that the cell tries to move along its direction of internal biochemical polarity. Alignment to the polarity is modulated by the alignment rate χ , which we think of as reflecting the rate at which the cell's motility machinery reorients to reflect any underlying biochemical polarization $\hat{\mathbf{p}}$. The χ term is essential for galvanotaxis, as we assume the electric field alters the polarity $\hat{\mathbf{p}}$. The last term on the right is a rotational noise: $\xi(t)$ is a Gaussian Langevin noise with $\langle \xi(t) \rangle = 0$ and $\langle \xi(t_1)\xi(t_2) \rangle = \delta(t_1 - t_2)$. $\hat{\mathbf{v}}_{\perp}$ is a unit vector perpendicular to \mathbf{v} . The noise accounts for the aggregate effect of noisiness in signal transduction [49] and motility [50, 51].

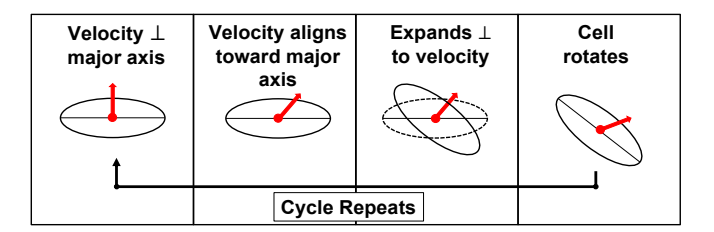


FIG. 2: Schematic of the interaction between two competing processes: velocity alignment to the long axis and shape expansion perpendicular to the velocity. This competition leads to circular motion of the cell.

Cell shape $S_{\alpha\beta}$ obeys, following [24] exactly:

$$\frac{\mathrm{d}S_{\alpha\beta}}{\mathrm{d}t} = -\kappa S_{\alpha\beta} - b\left(v_{\alpha}v_{\beta} - \frac{1}{2}v^{2}\delta_{\alpha\beta}\right). \tag{3}$$

The first term in this equation informs us that elongated shapes tend to relax back to a circular shape with a rate κ – similar to the role of cell tension in [17]. Steady-state

circular shapes have been observed in nonmotile keratocyte lamellipodial fragments [52, 53] – consistent with Eq. 3, where the circular state is stable when the cell is motionless. The second term on the right of Eq. 3 models cell shape responding to cell velocity, and was proposed by [24] as the simplest term coupling the components of velocity v_{α} to the shape tensor $S_{\alpha\beta}$ allowed by symmetry – we must set b as a phenomenological parameter. However, we note that because b reflects the change in cell shape in response to local protrusive and contractile signals, it will reflect the strength and distribution of those signals around the cell perimeter – see, e.g. [42, 54, 55]. If b < 0, cells expand their shape perpendicular to the direction of the velocity and contract parallel to the velocity. Cells expanding perpendicular to motion directly competes with \mathbf{v} aligning with $\pm \hat{\mathbf{n}}$ whenever shape or velocity changes rapidly, leading to rotation and oscillations (Fig. 2). We emphasize that the cell generally ends up with its velocity perpendicular to $\hat{\mathbf{n}}$, but velocity orientation can be transiently different during turns and oscillations. As keratocytes have their long axis perpendicular to the direction of travel, we will have b < 0throughout the main paper. We show some results for cell types that travel parallel to their long axis, choosing a, b > 0 in Appendix E.

Lastly, the time evolution of the angle of the polarity, $\hat{\mathbf{p}} = (\cos \phi_{\mathbf{p}}, \sin \phi_{\mathbf{p}})$, is given by:

$$\frac{\mathrm{d}\phi_{\mathrm{p}}}{\mathrm{d}t} = -\frac{1}{\tau}\arcsin\left[(\hat{\mathbf{v}}\times\hat{\mathbf{p}})_z\right] - \frac{1}{\tau_{\mathrm{b}}}\arcsin\left[(\hat{\mathbf{E}}\times\hat{\mathbf{p}})_z\right] + \sigma_{\mathrm{p}}\xi_{\mathrm{p}}(t).$$
(4)

The first term here aligns the cell's polarity with its velocity over a timescale τ i.e. a cell will want to polarize along its direction of travel [56–60]. The second term similarly shows that the polarity tends to align to the electric field's direction **E** over a timescale $\tau_{\rm b}$. $\tau_{\rm b}$ reflects the timescale for a cell to become polarized in response to an electric field, potentially by membrane proteins redistributing on the cell surface [20, 25, 61, 62]. The $\tau_{\rm b}$ term in the polarity equation is the only role of the electric field within our model. The term $\xi_{\rm p}$ is a Gaussian Langevin noise with zero mean and $\langle \xi_{\mathbf{p}}(t_1)\xi_{\mathbf{p}}(t_2)\rangle = \delta(t_1 - t_2)$. Noise in polarity could arise from the finite number of sensing proteins [62], stochastic conformation changes of relevant ion channels [63, 64], or finite numbers of signaling molecules [65, 66]. Within our model, we only include the electric field's direction – we do not explicitly include its magnitude, which could alter the timescale over which the polarity aligns with the bias $\tau_{\rm b}$.

We fit parameters to data in [20]; see Results (Section III) and Appendix B. We simulate our model equations (Eqs. 2-4) using the Euler-Maruyama method. To handle the noise $\xi(t)$ and $\xi_p(t)$ numerically, we defined a new Gaussian distributed random variable Γ :

$$\Gamma(\Delta t) = \int_{t}^{t+\Delta t} \xi(t) \, dt.$$

Using the delta-correlation of the noise, $\langle \Gamma \rangle = 0$ and $\langle \Gamma^2 \rangle = \Delta t$. That means numerically, $\Gamma = \mathcal{X} \sqrt{\Delta t}$, where

 $\mathcal{X} \sim \mathcal{N}(0,1)$. For an example of this approach, we integrate Eq. 2 from time t to $t + \Delta t$:

$$\mathbf{v}(t + \Delta t) - \mathbf{v}(t) = f(\mathbf{v}(t), \mathbf{\ddot{S}}(t), \mathbf{\hat{p}}(t)) \Delta t + \sigma \Gamma \mathbf{\hat{v}}_{\perp}(t).$$

Other equations are integrated similarly.

III. RESULTS

Phase diagram of model in absence of a field

We show the phases of cell motion in the absence of a field in Fig. 3A. With no field present and no noise, we observe two relevant steady states: cells may either travel in a straight line with their long axis perpendicular to their velocity, or move in a circular trajectory. Like the original work of [24], we observe a transition between perfectly straight, linear motion at small cell speeds (low γ) and large shape relaxation rates (large κ) and circular motion at large γ and small κ . We can identify this transition line by a linear stability analysis around the steady-state of a cell crawling in a straight line, neglecting noise (Appendix D). We find two transition lines γ_1 and γ_2 ,

$$\gamma_1 = \frac{\kappa^2}{ab} + \left(\frac{1}{2\mu} + \frac{\chi + \tau^{-1}}{ab}\right) \kappa + \frac{\chi + \tau^{-1}}{2\mu},$$
(5)

$$\gamma_2 = \frac{\chi \tau + 1}{ab} \kappa^2 + \frac{\chi \tau + 1}{2\mu} \kappa. \tag{6}$$

Linear motion is stable to perturbations if $\gamma < \min(\gamma_1, \gamma_2)$. Once $\gamma > \gamma_1$ or γ_2 , then linear motion is unstable. We mark the region of the phase diagram Fig. 3A where linear motion is stable as "Persistent Motion Stable."

The phase diagram is plotted with respect to the "wild-type" parameters, the default fitted values for our model parameters. We found these parameters from fitting our model to data from [20] showing cells' response to a field being turned on (Appendix B and Fig. 4).

In Fig. 3A, we highlight three points on the phase diagram and show example trajectories. The curve in Fig. 3A is simply γ_2 , because $\gamma_2 < \gamma_1$ in the region of parameter space presented. Unlike the phase diagram, which was constructed without noise, the example trajectories have noise. In the presence of noise, the orientation of the cell changes even in the linear motion phase, and the cell undergoes a persistent random walk due to its orientational fluctuations. Thus, we define linear motion as characterized by perfectly straight cell migration without noise. Meanwhile, persistent motion is the analog of linear notion in the presence of noise, characterized by a persistent random walk with no loops, turns, or oscillations. We see in Fig. 3A that our wild-type values, represented by point i, are slightly above the transition line, where linear/persistent motion is unstable; meaning

that the cell would exhibit circular motion/noisy trajectory with loops, turns, and oscillations. At the wild-type parameters, we see cell trajectories that resemble "knots on a string" [18], where the cell goes through episodes of circular movement (Fig. 3i, Movie S1). The wild-type values being right above the transition line is due to an assumption in our fitting process: because both circular and persistent motion are observed in normal keratocytes, reasonable parameters must be close to the transition (Appendix B).

As we move away from the transition line and increase cell speed by increasing γ (Fig. 3ii, Movie S2), we see that the cell travels perpetually in a circle, slightly perturbed by noise. Circular crawling is seen in keratocytes in [18], though our model can produce trajectories – like Fig. 3ii – with tighter loops than biologically observed. If we move across the transition by increasing cell shape relaxation rate κ (Fig. 3iii, Movie S3), we see that persistent migratory motion is stabilized again. While the boundary derived from Eqs. 5 and 6 is determined without added noise, it nonetheless captures a key transition in the model between persistent and circular migration.

How do the phenotypes seen in Fig. 3A relate to the cell's ability to explore space? We plot the mean squared displacement over time in Fig. S2 for the parameter sets in Fig. 3Ai, ii and iii. We see transition between persistent and diffusive motion over one hour for wild-type i, oscillations for ii, and highly persistent motion for iii.

Field stabilizes cell response

Fig. 3A shows cell behaviors in the absence of a field. Fig. 3B shows how these phases can change in the presence of a field. In our simulations, we noticed that unstable linear motion can be stabilized with a field (Movie S4), depending on where we are in parameter space. We extended our linear stability analysis to the case with a field present with no noise (Appendix D). The linear stability curves are shown in the lines in Fig. 3B, where the solid line demarcates the transition between unstable linear motion and stable linear motion in the absence of an electric field, and the dotted line demarcates the transition in the *presence* of an electric field. However, even if the straight trajectory is linearly unstable, the cell may still be able to follow the field. The linear stability analysis shows whether the linear trajectory following the field is stable to small perturbations – and at the wildtype parameters, it is not. Fig. 3iv shows an example of a trajectory from the phase diagram using our wild-type parameters (this trajectory, like all our plotted example trajectories, includes the stochastic noise terms). In Fig. 3iv, the field is on, but persistent motion is unstable. This is apparent by the presence of loops, turns, and oscillations. It is crucial to note that cells in the regime of globally unstable linear motion, such as Fig. 3iv, clearly can still follow a field. However, once we move across the solid transition line by increasing the rate χ that \mathbf{v} aligns

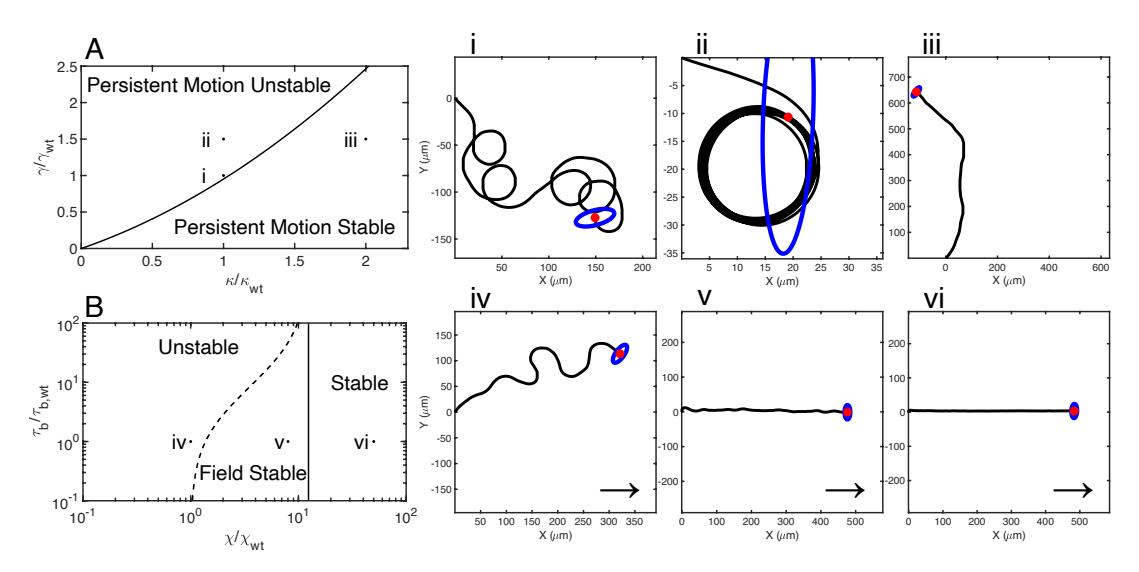


FIG. 3: (A): Linear stability phase diagram in $\gamma - \kappa$ plane in the absence of electric field. Example trajectories for points i-iii are shown. (i): shows a 2.5-hour trajectory at the "wild-type" (WT) values, $(\gamma = \gamma_{\rm wt}, \ \kappa = \kappa_{\rm wt})$. (ii): 1-hour trajectory when cell speed is increased, resulting in persistent circular motion, $(\gamma = 1.5\gamma_{\rm wt}, \ \kappa = \kappa_{\rm wt})$. (iii): 1.5-hour trajectory with increased shape relaxation rate κ shows persistent random walk, $(\gamma = 1.5\gamma_{\rm wt}, \ \kappa = 2\kappa_{\rm wt})$. (B): Linear stability phase diagram in $\tau_{\rm b} - \chi$ plane. Transition lines in presence of field (solid line) and absence (dotted line) are shown, and examples iv-vi are shown with field. (iv): 1.5-hour WT trajectory following a field in $+\hat{\mathbf{x}}$ -direction. In this region of the plot, persistent motion is unstable, but the cell oscillates side to side while traveling in the field direction. (v): 1.5-hour trajectory following an field pointing in $+\hat{\mathbf{x}}$ -direction. In this region of the plot, persistent motion is stabilized in the presence of a field and there are no oscillations, $(\tau_{\rm b} = \tau_{\rm b, wt}, \ \chi = 8\chi_{\rm wt})$. (vi): 1.5-hour trajectory following an field pointing in $+\hat{\mathbf{x}}$ -direction, $(\tau_{\rm b} = \tau_{\rm b, wt}, \ \chi = 50\chi_{\rm wt})$.

with $\hat{\mathbf{p}}$, linear motion is unstable only in the absence of a field, meaning that a cell would migrate persistently without oscillations when a field is present. We then see the oscillations around the field direction disappear in Fig. 3v. Once we cross the dotted transition line by increasing the rate of $\mathbf{v} - \hat{\mathbf{p}}$ alignment further, Fig. 3vi shows us a cell following the field even more persistently.

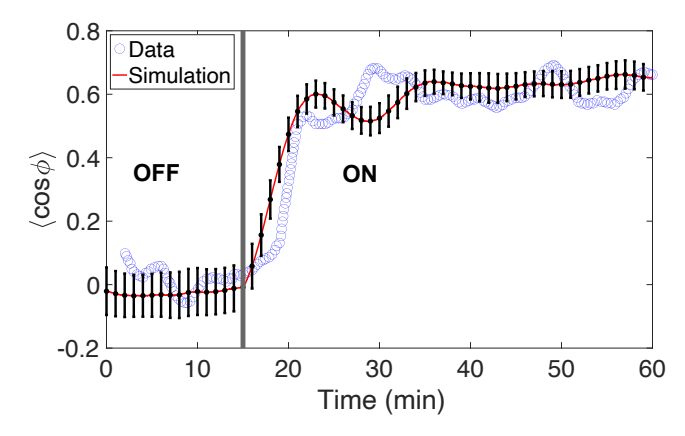


FIG. 4: Cell response to a field being turned on. Here, ϕ is the angle of the cell's velocity with respect to the field direction, and the field is turned on at 15 minutes. In blue is experimental data of the average response of 140 cells, extracted from [20]. In red is our simulation data which we fit to experiment to calibrate our parameters, averaging over 1000 cells. Error bars are ± 1 standard deviation of the average, computed by bootstrapping (Appendix B).

Simulations recapitulate experimental response to field

To validate our model parameters and determine their wild-type values, we fit our simulations to data from Allen et al. (2013) [20]. This data, shown in blue dots in Fig. 4, shows the experimental data of the average response of 140 cells responding to a field being switched on after 15 minutes of no exposure. We simulated 1000 cells freely traveling, responding to a field pointing in the $+\hat{\mathbf{x}}$ -direction that is switched on after 15 minutes. In Fig. 4, we plot the average response of those 1000 cells as directedness vs. time in minutes. The directedness is defined by $\langle \cos \phi \rangle$, where ϕ is the angle of the cell velocity relative to the field. For the first 15 minutes when no field is present, we observe cells on average to go in all directions, so $\langle \cos \phi \rangle \approx 0$. Once the field turns on, the cells in the experiment respond to the field and follow it to varying levels of precision. In the figure, we see the directedness leveling off at $\langle \cos \phi \rangle \approx 0.6$. This reflects both orientational noise and cell trajectories that often oscillate around the field direction (Fig. 3iv). Details of the fit, including how we tuned our parameters are discussed in Appendix B.

Our model captures the experimentally observed response to a field being switched on reasonably well. What parameters influence this response and to what degree?

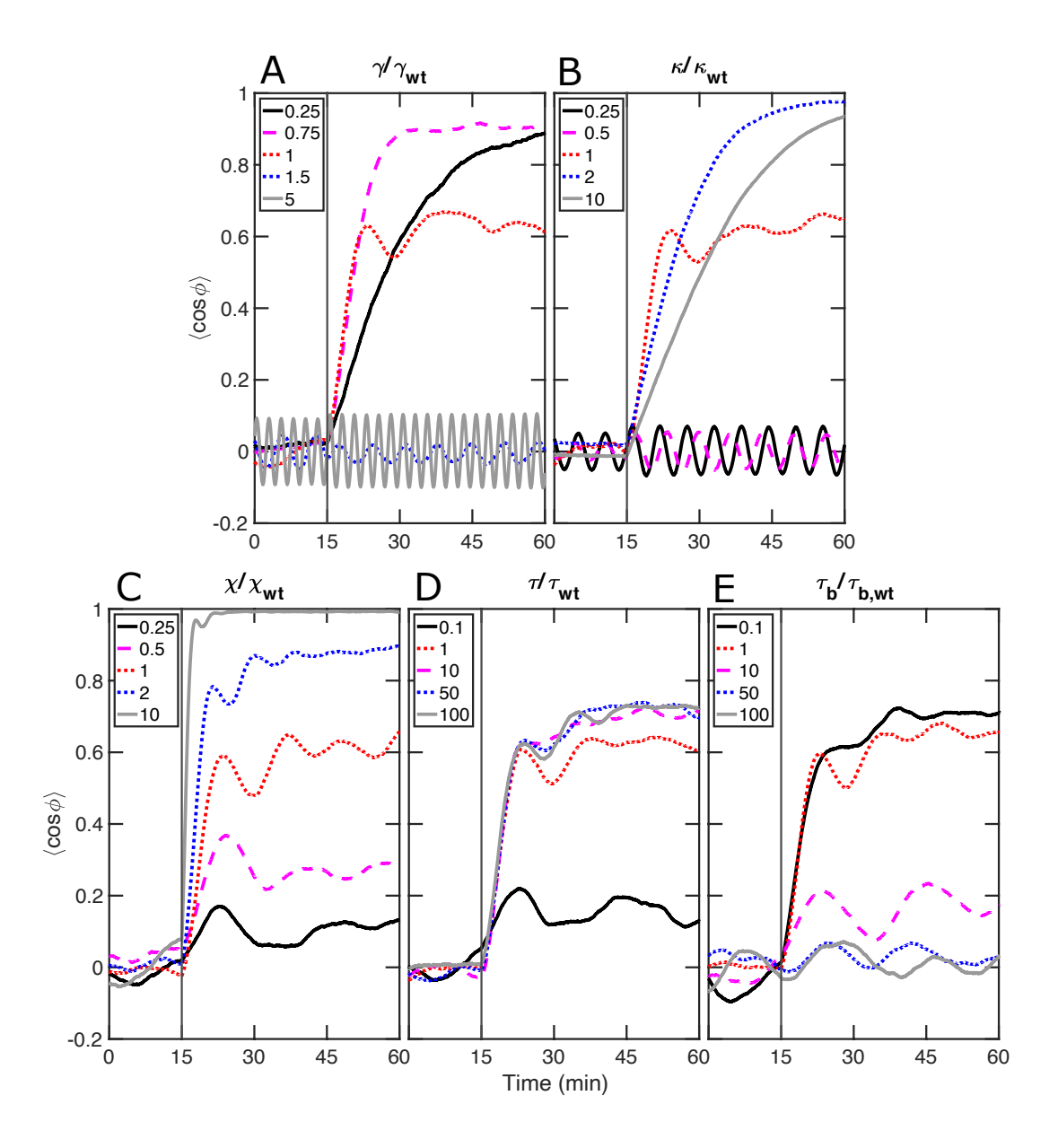


FIG. 5: Response to a field being turned on at 15 minutes, as in Fig. 4, with parameters varied from fit wild-type parameters. (**A**): speed parameter γ . (**B**): shape relaxation rate κ . (**C**): velocity to polarity alignment rate χ . (**D**): polarity to velocity alignment time τ . (**E**): field alignment time τ_b . Each curve is the average response of 500 cells. Error bars are not shown in order to preserve clarity, but curve-to-curve variability is limited (see dotted red wild-type curve from panel to panel).

Cell speed, shape, and ability to align with field control cell response to field activation

In Fig. 5 we use the cell directedness $\langle\cos\phi\rangle$ in response to a field being turned on for various parameter values. Fig. 5 demonstrates how cell responses to an electric field would change if we looked at cells with different speeds, shape relaxation rates, rates of alignment to the field, etc. We vary parameters values relative to the wild-type model fit parameters (Table I). We see that cells with lower speeds, $\gamma < \gamma_{\rm wt}$, have a more reliable response – their value of $\langle\cos\phi\rangle$ saturates to a value of

 ~ 0.9 , compared to ~ 0.6 for the wild-type cells (Fig. 5A). However, this may come at a cost: for a slow enough cell, $\gamma = 0.25\gamma_{\rm wt}$, the response to a field turned on at 15 minutes takes over 45 minutes to reach its steady-state level. This behavior is closely linked to where the cell's parameters are in the phase diagram (Fig. 3). For speeds much above the wild-type speed, e.g. $\gamma = 1.5\gamma_{\rm wt}$, cells undergo a mostly circular trajectory and there is no net directedness (though there can be drift perpendicular to the field; see discussion of Fig. 6). Based on our linear stability results, we would expect that increasing the rate of shape relaxation κ would make linear, persistent mo-

tion more stable, allowing for a more directed response. This is what we find (Fig. 5B): increasing κ leads to a more directed response (saturation value of $\langle \cos \phi \rangle$ nearing 1). Similarly to our results for cell speed, increasing shape relaxation rate κ can both increase the accuracy and slow the response time (see $\kappa = 10\kappa_{\rm wt}$ curve).

In our model, the electric field reorients cell polarity $\hat{\mathbf{p}}$ – but for the cell's actual motility to reflect this change in polarity, the coupling between polarity and velocity is essential. The rate of this coupling is χ . We see that if we decrease χ below the wild-type value, the response to signal becomes systematically less directed (Fig. 5C). However, increasing χ can simultaneously increase accuracy and the response time of cells – increasing χ to $10\chi_{\rm wt}$ results in a cell that reaches near-perfect alignment with the field in under five minutes. This suggests that, with our fit parameters, bringing the velocity in alignment with the polarity can be the slowest element of cell reorientation. This is consistent with the small value of the time scale $\tau_{\rm b}$: polarity aligns with the field in much less than a minute.

We have also modeled an alignment of cell polarity back to cell velocity ("self-alignment" [56, 57, 60, 67]), which occurs with timescale τ . Self-alignment appears to not be essential to cell response. Increasing τ (reducing the influence of self-alignment) even by orders of magnitude does not have a large effect on directionality (Fig. 5D). By contrast, if τ is decreased to the order of τ_b , e.g. at $\tau = 0.1\tau_{\rm wt}$, the cell's polarity must compromise between the field direction and the current velocity, and the cell responds more slowly and has a low directedness saturation level.

Our model has the cell polarity align to the field over a timescale $\tau_{\rm b}$, subject to stochastic noise. Increasing $\tau_{\rm b}$ should then reduce the influence of the electric field. By increasing $\tau_{\rm b}$ sufficiently ($\tau_{\rm b}=50\tau_{\rm b,wt}$) we can nullify cell response to the field entirely (Fig. 5E). Because $\tau_{\rm b}$ controls cell repolarization to the field, we would naively expect decreasing $\tau_{\rm b}$ below the wild-type to make the cell response to field turn-on faster. However, instead we see little effect of setting $\tau_{\rm b}=0.1\tau_{\rm b,wt}$, suggesting that the reorientation of polarity to the field is not rate-limiting – sensible as $\tau_{\rm b,wt}\approx 1.4$ seconds, far less than the timescale for cell reorientation. The relative unimportance of $\tau_{\rm b}$ is consistent with the importance of χ : solely increasing χ can make cells respond in < 5 minutes.

Cell response to switching fields includes averaging, tracking, and more complex behaviors

Our results in Fig. 4 and 5 show how a cell responds to a field that is switched on and kept in a fixed direction. Fig. 6 illustrates the results we see when we observe how a cell responds to a field being continually switched between the $+\hat{\mathbf{x}}$ - and $+\hat{\mathbf{y}}$ -directions. This is motivated by the experiments of Zajdel *et al.* [34], who probed collective cell migratory response to a rapidly switching

electric field (Fig. 6A). They discovered that on short time scales (20 seconds) the group of cells time average the varying field and follow the composite direction. For example, if a field switches from $+\hat{\mathbf{x}}$ and $+\hat{\mathbf{y}}$, cells travel in a 45 degree angle. However, on longer times, cells follow the field direction reliably.

When single cells respond to time-varying fields, do they track it closely (Fig. 6C, Movie S5) or average the field (Fig. 6D, Movie S6)? The experimental results of [34] and our results of Fig. 5 suggest that when a field is switched on, there is a delay in response, which affects how well a cell would track or average a field. We know some of the parameters that control this response delay. To what degree do these parameters control responses to a changing field? On what time scale is a switching field considered "rapid"?

In Fig. 6, we show how cells respond to a switching electric field. During each simulation, we vary the direction of the field from $+\hat{\mathbf{x}}$ to $+\hat{\mathbf{y}}$ every t_{ET} minutes - the "exposure time" (Fig. 6A). $t_{\rm ET}$ is held constant throughout a single simulation. We show results for how the cell behavior varies with exposure time, varying exposure time over 60 values from $t_{\rm ET}=2.5$ minutes to 2.5 hours. We show in Fig. 6B the cell's response to a switching field as a function of exposure time by showing the probability density of the cell velocity's angle ϕ_{cell} . We plot this angle relative to the reference angle of 45°, $\phi_{\rm r} = \pi/4$, which the cell would take if the cell averaged the signal perfectly (we compute the angles of the velocity averaged over the exposure time; see Appendix F). We anticipated that a cell would take the average of a dynamically changing field at short exposure times, when the cell could not adequately respond in the timescale of the changing field. In this case, the cell should travel along $\phi_{\rm r} = \pi/4$. However, when the exposure time is much longer than the cellular response time (typically on the order of 10 minutes), we would expect that the cell tracks the changing field direction, producing a staircaselike trajectory. Fig. 6B shows heat maps to illustrate this result. Here, $\Delta \phi = \phi_{\rm cell} - \phi_r$. A cell traveling along the diagonal $\phi_{\rm r} = \pi/4$ would produce a heat plot with density centered at $\Delta \phi = 0$. We highlight this point with a solid red line. However, as the exposure time increases. we would expect to see two distinct bands at $\Delta \phi = \pm \pi/4$ (dashed red lines), a sign that $\phi_{\text{cell}} = \{0, \pi/2\}$, indicating that the cell is traveling in a staircase pattern (Fig. 6C). This characteristic shape is seen most clearly in Fig. 6B when $\kappa = 10\kappa_{\rm wt}$. This is consistent with the response to a field turning on at $\kappa = 10\kappa_{\rm wt}$ seen in Fig. 5B, where we see a very high level of cell directedness, but a slow response. Hence, we expect cells would not be able to follow a field with a short switching time, but would track reliably at long exposure times, forming solid bands at $\pm \pi/4$. However, this branching response is not as evident in the other parameters shown in Fig. 6B. The heat map for $\chi = 10\chi_{\rm wt}$ is similar, but shows two clear bands at nearly all exposure times except the shortest ones – there is no averaging unless the field is switched less than

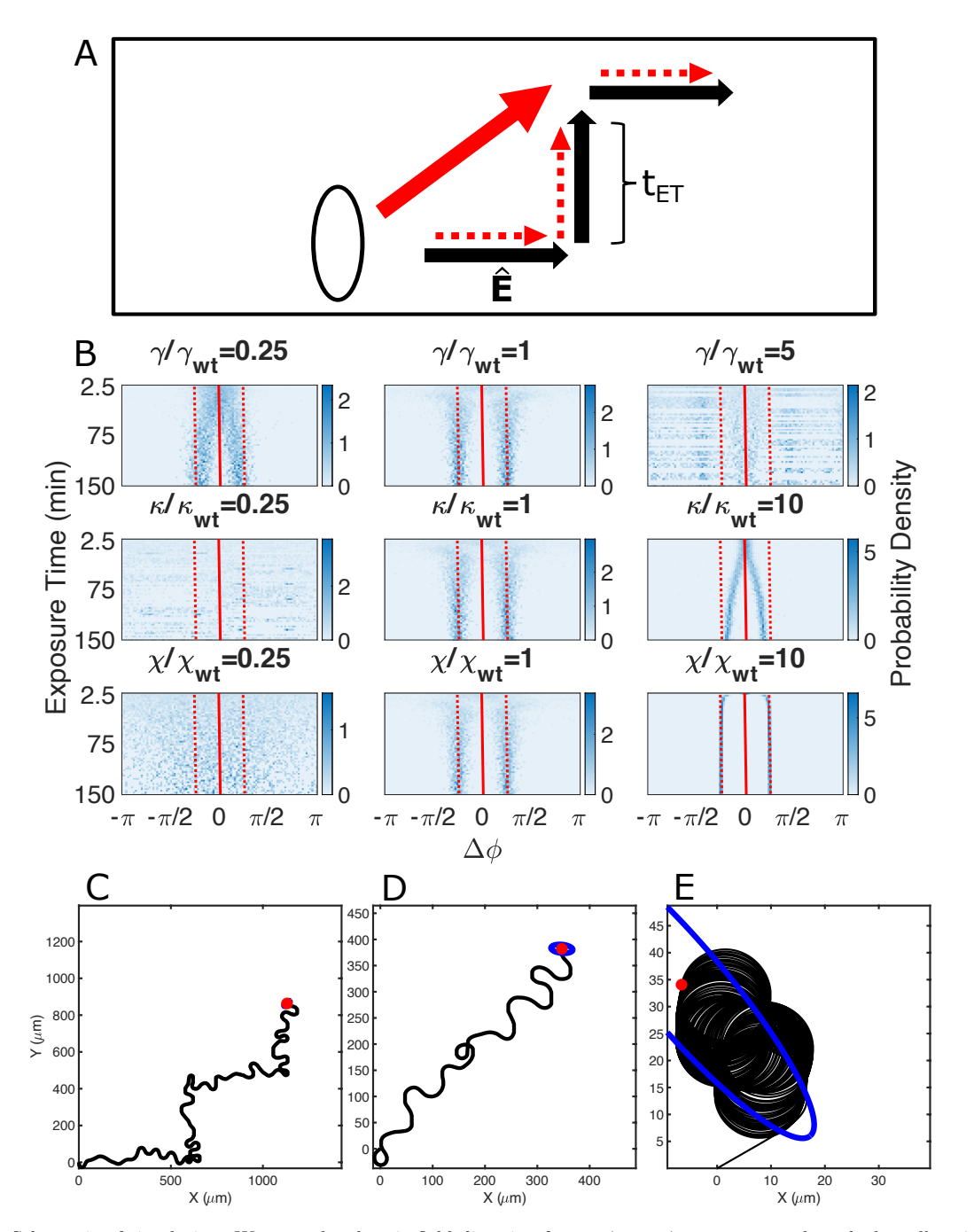


FIG. 6: (A): Schematic of simulation. We vary the electric field direction from $+\hat{\mathbf{x}}$ to $+\hat{\mathbf{y}}$ every $t_{\rm ET}$ and track the cell trajectory. Will the cell follow the field closely (dotted red arrows) or average the field directions (solid red arrow)? (B): Probability density plots. These are histogram heatmaps indicating the probability of a cell averaging and pointing in the composite direction of the two field directions $(+\hat{\mathbf{x}}$ and $+\hat{\mathbf{y}})$ versus pointing in the field directions directly. Simulations are done for 100 simulation hours. The red lines correlate with the red arrows in (A). Center solid red line corresponds to a cell traveling on average around the average field direction. Dotted red lines corresponds to a cell following the field direction precisely. (C): 10-hour wild-type trajectory with slow switching time (2.5 hours). (D): 3-hour wild-type trajectory with fast switching time (5 minutes). (E): 4-hour trajectory with high γ value where cell rotates faster than our averaging sample time.

every 5 minutes. Again, this is consistent with Fig. 5C, where high values of χ have a response time of < 5 minutes and a highly directed response. $\gamma = 0.25 \gamma_{\rm wt}$ has a heatmap with a forking pattern, but the noise blurs the bands since the cell does not follow and respond to the field as strongly, consistent with Fig. 5A.

The middle panels of Fig. 6B all show heatmaps at the wild-type parameter values, however, like $\gamma = \gamma_{\rm wt} 0.25$, the heatmaps look blurred at short exposure times, though there are clear peaks at $\pm \pi/4$ at longer exposure times. The behavior at short exposure time shows a broad distribution of angles $\Delta \phi$, but with a peak at zero,

indicating that the cell is most commonly going in the expected direction ϕ_r . Fig. 6C and D show representative examples of trajectories at the wild-type parameters when the field is switched at 2.5 hours and 5 minutes, respectively (see also Movies S5 and S6).

Even with a field on, we observe some parameter values where cells move in circles, which leads to strange results in the corresponding heatmaps in Fig. 6B. For $\gamma = 5\gamma_{\rm wt}$ and $\kappa = 0.25\kappa_{\rm wt}$, we do not see a branching pattern nor do we see peaks at $\Delta \phi = \pm \pi/4$, as the cell is rotating – which can be seen in Fig. 5A and B as oscillations in the directionality. This rapid rotation does follow a sort of staircase pattern (Fig. 6E, Movie S7) – but does not result in a net movement in the direction of the fields. In this regime, the rotating cell body moves perpendicular to the field direction. Depending on the direction of the cell's rotation (clockwise or counter-clockwise), the cell will then move in different directions in the field. In this example where the cell rotates counterclockwise, the cell's center of mass drifts in the $+\hat{\mathbf{v}}$ -direction when the field points in the $\hat{\mathbf{x}}$ -direction, and the cell drifts in the $-\hat{\mathbf{x}}$ -direction when the field points in $+\hat{\mathbf{y}}$. When the cell rotates clockwise, the drifts will be in the opposite direction. This rotational motion explains the patchy structure of the heat maps of $\gamma = 5\gamma_{\rm wt}$ and $\kappa = 0.25\kappa_{\rm wt}$: they are constructed from one long simulation, where the cell spontaneously breaks symmetry from its initial conditions, ending up rotating clockwise or counter-clockwise, setting its direction of net drift. Therefore, we see either a large density at $\Delta \phi > 0$ or $\Delta \phi < 0$, which changes from one exposure time to another. We see from this that the influence of our stochastic noise is attenuated at these extreme parameter values, as the cell's initial symmetry breaking persists over the length of the trajectory. We emphasize that the behavior seen in Fig. 6E and Movie S7 is an extreme edge case of our model that has yet to be experimentally validated as there is no experimental evidence of cell drift depending on rotation in galvano-

For the parameter set $\chi = 0.25\chi_{\rm wt}$, cells are much less effective at following the field (Fig. 5C), and we do not see a strong directed response in the heat maps. This is also in the regime where cells are experiencing episodes of rotation, albeit not always in a perfectly circular pattern (Movie S8). However, the heat map is not as patchy as the heat maps for $\gamma = 5\gamma_{\rm wt}$ and $\kappa = 0.25\kappa_{\rm wt}$. Instead of seeing larger densities at $\Delta \phi > 0$ or $\Delta \phi < 0$, we see a more uniform distribution with slight densities near $\Delta \phi = \pi/4$ or $\Delta \phi = -\pi/4$ at longer exposure times. This is due to the slower rotation and less directed motion in this regime. Hence, this regime has a greater sensitivity to noise. We are plotting the direction averaged over the exposure time. For $\gamma = 5\gamma_{\rm wt}$, $\kappa = 0.25\kappa_{\rm wt}$, cells often are able to perform several circular motions per averaging period – so the average angle picks up on the net drift. Slower rotations, as in $\chi = 0.25\chi_{\rm wt}$, lead to less directed velocities. Therefore, we don't see analogous patchy bands in the $\chi = 0.25 \chi_{\rm wt}$ case.

IV. DISCUSSION

Our model recapitulates several qualitative migration behaviors observed in single keratocyte cells in or out of a field, including straight linear motion, persistent turning, turning while following a field (Fig. 3iv), and more complex "knots on a string" dynamics (Fig. 3i). These behaviors occur at slightly different parameter points in our model, but they can be created from relatively small changes in parameters – so we expect keratocytes, which have a broad distribution of different properties including speed and aspect ratio, would naturally exhibit all of the phases shown in Fig. 3. This results from our initial assumption that wild-type model parameters had to be near the transition calculated from the linear stability analysis.

Our model can make predictions beyond mimicking the aforementioned behaviors. In Figs. 4 and 5, our cell directionality responses to a field being turned on show an increase in directionality, but also subsequent "ringing" akin to a damped harmonic oscillator. There is a noticeable bump in Fig. 4 at ~ 22 minutes which stems from cells overcorrecting when responding to an electric field (Movie S9). A similar overcorrection is seen experimentally in single keratocyte trajectories (e.g. Fig. 3E of [18]), though it is not as immediately obvious in the averaged experimental data in Fig. 4, perhaps due to averaging of many cells with varying frequencies. Unsurprisingly, the degree of overcorrection increases for cells that initially face away from an electric field when it is turned on (Fig. S3) [20]. Earlier modeling of keratinocytes as a proportional controller leads solely to overdamped, nonoscillatory responses [68]. In our model, the presence of the ringing depends on the nearness to the circular motion transition line. We would then think of parameters like $1/\gamma$ and κ as analogous to friction coefficients in a damped harmonic oscillator, where smaller cell speeds (large $1/\gamma$) and greater shape relaxation rates (large κ) attenuate oscillations. Other parameters like χ and τ may also play a role.

We have only studied cells in the presence or absence of a field, and have not systematically varied the strength of the field, which is not explicitly invoked in our model. Within our model, the role of the field is only to reorient the cell polarity. It is also possible that electric fields could have effects on single cells beyond repolarization, such as an increase in cell speed (electrokinesis). There is some evidence that stronger electric fields increases cell speed for neural progenitor cells and 3T3 fibroblasts [69, 70]. Stronger fields have also been observed to increase directedness and decrease response times of keratocytes [14, 15, 20]. However, these results may be difficult to interpret. While Allen et al. [20] did observe a positive correlation between keratocyte speed and field strength – they also noted that the increase in voltage led to an increase in temperature, which separately increases cell speed [71]. This makes it difficult to discern if electric fields can increase cell speed alone. Possibilities for

the effects of electric fields on single cells including electrokinesis have been systematically studied by Prescott et al., in experiments on human corneal epithelial cells, who found that the only consistent model was one where cells preferentially polarize in the direction of the field [72], supporting our broad assumptions about the polarity. We should note that if cell speeds changed as a function of field strength (i.e. making γ a function of $|\mathbf{E}|$), this could lead to dramatic changes in single-cell response (Fig. 5A). We argue that the most natural interpretation of our model to study field strength systematically is to assume that the rate at which the polarity aligns with the field, $\tau_{\rm b}^{-1}$, could increase as the field increases. For our fit parameters, we predict relatively small changes from making the time τ_b smaller (Fig. 5E) – suggesting that increasing field strength beyond 1 V/cm (the field used in the experimental data shown in Fig. 4) would not directly increase taxis, but that dropping the field could lead to impaired directionality.

In principle, the time τ_b should reflect the time the cell takes to develop an underlying biochemical polarity in response to an electric field, e.g. by charged proteins on the membrane's surface electromigrating. However, the timescale of electromigration is much slower than the ~ 1.4 second value we find for τ_b [20, 62]. This could mean that we should think of the polarity $\hat{\bf p}$ as indicating a faster-responding cue than simple electromigration. However, an alternate possibility is that in our fitting, since the experimental data only measures cell velocity, the fit cannot distinguish between changes of polarity $\hat{\bf p}$ in response to the field and direct changes of the direction of ${\bf v}$ in response to the field – i.e. the slow electromigration response may largely be reflected in the value of $1/\chi \approx 14$ minutes, rather than τ_b .

The coupling between cell motion and cell shape is a core element of our model, which drives persistent circular motion and oscillation. This coupling could arise through the dynamics of Rho GTPases within the cell [17, 47], and similar effects can be generated through actomyosin instabilities [22]. How can experimental interventions be interpreted in our minimal model without these elements? κ is a suitable parameter for this interpretation. κ is the rate of cell shape relaxation from an ellipse to a circle. Our model trajectories reveal that a cell with a slower rate of shape relaxation (transitioning from large κ to $\kappa_{\rm wt}$) can hold an elongated shape for longer periods of time. Slower shape relaxation allows the cell to respond to cues and perturbations more quickly; however, it tends to sacrifice accuracy in following these cues and perturbations (Fig. 5). We find that more elongated cells with small values of κ turn more quickly (Fig. 5). However, when $\kappa \ll \kappa_{\rm wt}$, cells begin to oscillate. Lee et al. observed that cells with myosin activity inhibited by blebbistatin (low contractility) were less likely to oscillate [16], developing a model in which unequal amounts of adhesion on the left and right sides of the cell driven by myosin contractility destabilize linear motion, causing the cell to oscillate. It would be natural to assume that our shape relaxation rate κ would increase with contractility. This leads to a contradiction with [16], as we see oscillation at low κ , not high contractility. However, blebbistatin has other effects on cell motility, including changing cell speed [73]. In our model, reduction in cell speed stabilizes linear motion (Fig. 3). Thus, the blebbistatin treatments in [16] may not be straightforward to predict.

Zajdel et al. [34] studied how collections of MDCK kidney epithelial cell line and primary, neonatal mouse skin keratinocytes respond to a rapidly changing field. They saw that at exposure times of 10 seconds, a group of cells would average the field and follow the composite direction, but would follow a staircase pattern for longer exposure times of 1.5 hours. Our results are broadly in agreement with Zajdel et al. in the regime where persistent motion is stable. $\kappa = 10\kappa_{\rm wt}$ is a very clear example. The "wishbone" pattern clearly shows that at small time scales, we see the cell averaging and taking the composite field, but at large time scales, we see a cell follow a staircase pattern. The branching point of the wishbone is determined by the cell response time, which is determined by the transition region in the directedness vs. time plots (Fig. 5), the region where the graph has a sharp incline before saturating at steady value of $\langle \cos \phi \rangle$. Other heat maps show similar behavior, but the level of noise masks the effects. For example, in the wildtype, the density at short time scales is centered at zero, but has a wide spread. Understanding to what extent these single-cell response curves influence the ability of cell groups to turn around is a future direction.

One striking prediction of our model is that, in extreme parameter ranges where cells undergo rapid rotation, they will travel perpendicularly to the field, with a directionality that depends on the cell's direction of rotation (Fig. 6E). In principle, this suggests it could be possible in vitro to use an electric field to separate cells that rotate clockwise versus counterclockwise. While we only see this behavior at extreme parameter values that do not map to experimentally validated conditions and where stochasticity becomes less important, our results show that this is possible, highlighting that this behavior is allowed by the symmetry of the system, when the clockwise/counter-clockwise rotation breaks the symmetry between $\pm \hat{\mathbf{y}}$ with the field in the $\hat{\mathbf{x}}$ -direction. This drift of single cells is similar to behavior observed in simulations of clusters of rotating cells following a chemical gradient [74].

AUTHOR CONTRIBUTIONS

Both IN and BAC designed research, performed research, analyzed data, and wrote the paper.

DECLARATION OF INTERESTS

The authors declare no competing interests.

ACKNOWLEDGMENTS

We thank Emiliano Perez Ipiña for a careful reading of the paper. We acknowledge support from NSF PHY 1915491 and NSF MCB 2119948. IN was supported by the Program of Molecular Biophysics 5T32GM135131-02. This research project was conducted using computational resources at the Maryland Advanced Research Computing Center (MARCC).

REFERENCES

- [1] Shuvasree SenGupta, Carole A Parent, and James E Bear. The principles of directed cell migration. *Nature Reviews Molecular Cell Biology*, pages 1–19, 2021.
- [2] Inge Kunzenbacher, Jürgen Bereiter-Hahn, Mary Osborn, and Klaus Weber. Dynamics of the cytoskeleton of epidermal cells in situ and in culture. *Cell and Tissue Research*, 222(2):445–457, 1982.
- [3] Kinneret Keren and Julie A Theriot. Biophysical aspects of actin-based cell motility in fish epithelial keratocytes. In Cell Motility, pages 31–58. Springer, 2008.
- [4] Gary P Radice. Locomotion and cell-substratum contacts of xenopus epidermal cells in vitro and in situ. *Journal of Cell Science*, 44(1):201–223, 1980.
- [5] E Du Bois-Reymond. Untersuchungen über tierische Elektrizität., 1849.
- [6] Colin D McCaig, Ann M Rajnicek, Bing Song, and Min Zhao. Controlling cell behavior electrically: current views and future potential. *Physiological Reviews*, 2005.
- [7] Thomas H Dietz, Leonard B Kirschner, and David Porter. The roles of sodium transport and anion permeability in generating transepithelial potential differences in larval salamanders. *Journal of Experimental Biology*, 46(1):85–96, 1967.
- [8] Maria E Mycielska and Mustafa BA Djamgoz. Cellular mechanisms of direct-current electric field effects: galvanotaxis and metastatic disease. *Journal of Cell Science*, 117(9):1631–1639, 2004.
- [9] Andrew S Kennard and Julie A Theriot. Osmolarity-independent electrical cues guide rapid response to injury in zebrafish epidermis. eLife, 9:e62386, 2020.
- $[10] \ \ Robert \ O \ \ Becker. \ \ The \ \ bioelectric \ factors \ in \ amphibian-limb \ regeneration. \ \ \textit{JBJS}, \ 43(5):643-656, \ 1961.$
- [11] Ying Li, Yu Gu, He Wang, Zhipeng Liu, Bing Song, and Tao Yin. Electric pulses can influence galvanotaxis of Dictyostelium discoideum. *BioMed Research International*, 2018, 2018.
- [12] TA Banks, PSB Luckman, JE Frith, and JJ Cooper-White. Effects of electric fields on human mesenchymal stem cell behaviour and morphology using a novel multichannel device. *Integrative Biology*, 7(6):693–712, 2015.
- [13] M Sugimoto, N Maeshige, H Honda, Y Yoshikawa, M Uemura, M Yamamoto, and H Terashi. Optimum microcurrent stimulation intensity for galvanotaxis in human fibroblasts. *Journal of Wound Care*, 21(1):5–10, 2012.
- [14] Yaohui Sun, Hao Do, Jing Gao, Ren Zhao, Min Zhao, and Alex Mogilner. Keratocyte fragments and cells utilize competing pathways to move in opposite directions in an electric field. *Current Biology*, 23(7):569–574, 2013.
- [15] Mark S Cooper and Manfred Schliwa. Motility of cultured fish epidermal cells in the presence and absence of direct current electric fields. The Journal of Cell Biology, 102(4):1384–1399, 1986.
- [16] Kun Chun Lee, Greg M Allen, Erin L Barnhart, Mark A Tsuchida, Cyrus A Wilson, Edgar Gutierrez, Alexander Groisman, Julie A Theriot, and Alex Mogilner. Modeling cell turning by mechanics at the cell rear. bioRxiv, 2020.
- [17] Brian A Camley, Yanxiang Zhao, Bo Li, Herbert Levine, and Wouter-Jan Rappel. Crawling and turning in a minimal reaction-diffusion cell motility model: Coupling cell shape and biochemistry. *Physical Review E*, 95(1):012401, 2017.
- [18] Greg M Allen, Kun Chun Lee, Erin L Barnhart, Mark A Tsuchida, Cyrus A Wilson, Edgar Gutierrez, Alexander Groisman, Julie A Theriot, and Alex Mogilner. Cell mechanics at the rear act to steer the direction of cell migration. Cell Systems, 11(3):286–299, 2020.
- [19] Alex Mogilner, Erin L Barnhart, and Kinneret Keren. Experiment, theory, and the keratocyte: An ode to a simple model for cell motility. In Seminars in Cell & Developmental Biology, volume 100, pages 143–151. Elsevier, 2020.
- [20] Greg M Allen, Alex Mogilner, and Julie A Theriot. Electrophoresis of cellular membrane components creates the directional cue guiding keratocyte galvanotaxis. *Current Biology*, 23(7):560–568, 2013.
- [21] Hans Gruler and Richard Nuccitelli. Neural crest cell galvanotaxis: new data and a novel approach to the analysis of both galvanotaxis and chemotaxis. Cell Motility and the Cytoskeleton, 19(2):121–133, 1991.
- [22] Masoud Nickaeen, Igor L Novak, Stephanie Pulford, Aaron Rumack, Jamie Brandon, Boris M Slepchenko, and Alex Mogilner. A free-boundary model of a motile cell explains turning behavior. PLoS Computational Biology, 13(11):e1005862, 2017.

- [23] Brian A Camley, Yanxiang Zhao, Bo Li, Herbert Levine, and Wouter-Jan Rappel. Periodic migration in a physical model of cells on micropatterns. *Physical Review Letters*, 111(15):158102, 2013.
- [24] Takao Ohta and Takahiro Ohkuma. Deformable Self-Propelled Particles. Physical Review Letters, 102(15):154101, 2009.
- [25] Brian M Kobylkevich, Anyesha Sarkar, Brady R Carlberg, Ling Huang, Suman Ranjit, David M Graham, and Mark A Messerli. Reversing the direction of galvanotaxis with controlled increases in boundary layer viscosity. *Physical Biology*, 15(3):036005, 2018.
- [26] Ken-ichi Nakajima, Kan Zhu, Yao-Hui Sun, Bence Hegyi, Qunli Zeng, Christopher J Murphy, J Victor Small, Ye Chen-Izu, Yoshihiro Izumiya, Josef M Penninger, et al. Kcnj15/kir4. 2 couples with polyamines to sense weak extracellular electric fields in galvanotaxis. *Nature Communications*, 6(1):1–10, 2015.
- [27] Bo-jian Lin, Shun-hao Tsao, Alex Chen, Shu-Kai Hu, Ling Chao, and Pen-hsiu Grace Chao. Lipid rafts sense and direct electric field-induced migration. *Proceedings of the National Academy of Sciences*, 114(32):8568–8573, 2017.
- [28] Qian Liu and Bing Song. Electric field regulated signaling pathways. The International Journal of Biochemistry & Cell Biology, 55:264-268, 2014.
- [29] Min Zhao. Electrical fields in wound healing—an overriding signal that directs cell migration. In Seminars in Cell & Developmental Biology, volume 20, pages 674–682. Elsevier, 2009.
- [30] Mark L Lalli and Anand R Asthagiri. Collective migration exhibits greater sensitivity but slower dynamics of alignment to applied electric fields. Cellular and Molecular Bioengineering, 8(2):247–257, 2015.
- [31] Yaohui Sun, Haicen Yue, Calina Copos, Kan Zhu, Yang Zhang, Xing Gao, Yuxin Sun, Brian Reid, Francis Lin, Min Zhao, et al. PI3K inhibition reverses migratory direction of single cells but not cell groups in electric field. *bioRxiv*, 2020.
- [32] Brian A Camley. Collective gradient sensing and chemotaxis: modeling and recent developments. *Journal of Physics: Condensed Matter*, 30(22):223001, 2018.
- [33] Li Li, Robert Hartley, Bjoern Reiss, Yaohui Sun, Jin Pu, Dan Wu, Francis Lin, Trung Hoang, Soichiro Yamada, Jianxin Jiang, et al. E-cadherin plays an essential role in collective directional migration of large epithelial sheets. *Cellular and Molecular Life Sciences*, 69(16):2779–2789, 2012.
- [34] Tom J Zajdel, Gawoon Shim, Linus Wang, Alejandro Rossello-Martinez, and Daniel J Cohen. SCHEEPDOG: programming electric cues to dynamically herd large-scale cell migration. *Cell Systems*, 10(6):506–514, 2020.
- [35] Gawoon Shim, Danelle Devenport, and Daniel J Cohen. Overriding native cell coordination enhances external programming of collective cell migration. *Proceedings of the National Academy of Sciences*, 118(29), 2021.
- [36] Jonathan Edward Dawson, Tina Sellmann, Katrin Porath, Rainer Bader, Ursula van Rienen, Revathi Appali, and Rüdiger Köhling. Computational model for migration of human osteoblasts in direct current electric field. bioRxiv, pages 2020–12, 2021.
- [37] T Hiraiwa, MY Matsuo, T Ohkuma, T Ohta, and M Sano. Dynamics of a deformable self-propelled domain. *EPL* (Europhysics Letters), 91(2):20001, 2010.
- [38] Tetsuya Hiraiwa, Akinori Baba, and Tatsuo Shibata. Theoretical model for cell migration with gradient sensing and shape deformation. The European Physical Journal E, 36(4):1–9, 2013.
- [39] Takao Ohta, Takahiro Ohkuma, and Kyohei Shitara. Deformation of a self-propelled domain in an excitable reaction-diffusion system. *Physical Review E*, 80(5):056203, 2009.
- [40] Takao Ohta, Mitsusuke Tarama, and Masaki Sano. Simple model of cell crawling. *Physica D: Nonlinear Phenomena*, 318:3–11, 2016.
- [41] Danahe Mohammed, Guillaume Charras, Eléonore Vercruysse, Marie Versaevel, Joséphine Lantoine, Laura Alaimo, Céline Bruyère, Marine Luciano, Karine Glinel, Geoffrey Delhaye, et al. Substrate area confinement is a key determinant of cell velocity in collective migration. *Nature Physics*, 15(8):858–866, 2019.
- [42] Kinneret Keren, Zachary Pincus, Greg M Allen, Erin L Barnhart, Gerard Marriott, Alex Mogilner, and Julie A Theriot. Mechanism of shape determination in motile cells. *Nature*, 453(7194):475–480, 2008.
- [43] Carlos Jurado, John R Haserick, and Juliet Lee. Slipping or gripping? fluorescent speckle microscopy in fish keratocytes reveals two different mechanisms for generating a retrograde flow of actin. *Molecular Biology of the Cell*, 16(2):507–518, 2005.
- [44] Yuan Zhong and Baohua Ji. Impact of cell shape on cell migration behavior on elastic substrate. *Biofabrication*, 5(1):015011, 2013.
- [45] Stephanie L Gupton and Clare M Waterman-Storer. Spatiotemporal feedback between actomyosin and focal-adhesion systems optimizes rapid cell migration. Cell, 125(7):1361–1374, 2006.
- [46] Lindsay B Case and Clare M Waterman. Integration of actin dynamics and cell adhesion by a three-dimensional, mechanosensitive molecular clutch. *Nature Cell Biology*, 17(8):955–963, 2015.
- [47] Amit R Singh, Travis Leadbetter, and Brian A Camley. Sensing the shape of a cell with reaction diffusion and energy minimization. Proceedings of the National Academy of Sciences, 119(31):e2121302119, 2022.
- [48] András Czirók, Eshel Ben-Jacob, Inon Cohen, and Tamás Vicsek. Formation of complex bacterial colonies via self-generated vortices. *Physical Review E*, 54(2):1791, 1996.
- [49] John E Ladbury and Stefan T Arold. Noise in cellular signaling pathways: causes and effects. Trends in Biochemical Sciences, 37(5):173–178, 2012.
- [50] David Selmeczi, Liwen Li, Lykke II Pedersen, SF Nrrelykke, Peter H Hagedorn, Stephan Mosler, Niels B Larsen, Edward C Cox, and Henrik Flyvbjerg. Cell motility as random motion: A review. The European Physical Journal Special Topics, 157(1):1–15, 2008.
- [51] Cynthia L Stokes, Douglas A Lauffenburger, and Stuart K Williams. Migration of individual microvessel endothelial cells: stochastic model and parameter measurement. *Journal of Cell Science*, 99(2):419–430, 1991.

- [52] Alexander B Verkhovsky, Tatyana M Svitkina, and Gary G Borisy. Self-polarization and directional motility of cytoplasm. Current Biology, 9(1):11–S1, 1999.
- [53] Michael M Kozlov and Alex Mogilner. Model of polarization and bistability of cell fragments. *Biophysical Journal*, 93(11):3811–3819, 2007.
- [54] Danying Shao, Herbert Levine, and Wouter-Jan Rappel. Coupling actin flow, adhesion, and morphology in a computational cell motility model. *Proceedings of the National Academy of Sciences*, 109(18):6851–6856, 2012.
- [55] Javier Satulovsky, Roger Lui, and Yu-li Wang. Exploring the control circuit of cell migration by mathematical modeling. Biophysical Journal, 94(9):3671–3683, 2008.
- [56] Balint Szabo, GJ Szöllösi, B Gönci, Zs Jurányi, David Selmeczi, and Tamás Vicsek. Phase transition in the collective migration of tissue cells: experiment and model. *Physical Review E*, 74(6):061908, 2006.
- [57] Brian A Camley and Wouter-Jan Rappel. Velocity alignment leads to high persistence in confined cells. Physical Review E, 89(6):062705, 2014.
- [58] András Szabó, R Ünnep, Eld Méhes, WO Twal, WS Argraves, Y Cao, and András Czirók. Collective cell motion in endothelial monolayers. *Physical Biology*, 7(4):046007, 2010.
- [59] Markus Basan, Jens Elgeti, Edouard Hannezo, Wouter-Jan Rappel, and Herbert Levine. Alignment of cellular motility forces with tissue flow as a mechanism for efficient wound healing. Proceedings of the National Academy of Sciences, 110(7):2452–2459, 2013.
- [60] Brian A Camley and Wouter-Jan Rappel. Physical models of collective cell motility: from cell to tissue. Journal of Physics D: Applied Physics, 50(11):113002, 2017.
- [61] S McLaughlin and MM Poo. The role of electro-osmosis in the electric-field-induced movement of charged macromolecules on the surfaces of cells. *Biophysical Journal*, 34(1):85–93, 1981.
- [62] Ifunanya Nwogbaga, A Hyun Kim, and Brian A Camley. Physical limits on galvanotaxis. arXiv preprint arXiv:2209.04742, 2022.
- [63] Alistair Mathie, L E. Kennard, and E L. Veale. Neuronal ion channels and their sensitivity to extremely low frequency weak electric field effects. *Radiation Protection Dosimetry*, 106(4):311–315, 2003.
- [64] Federico Bertagna, Rebecca Lewis, S Ravi P Silva, Johnjoe McFadden, and Kamalan Jeevaratnam. Effects of electromagnetic fields on neuronal ion channels: A systematic review. Annals of the New York Academy of Sciences, 1499(1):82–103, 2021.
- [65] Georg R Walther, Athanasius FM Marée, Leah Edelstein-Keshet, and Verônica A Grieneisen. Deterministic versus stochastic cell polarisation through wave-pinning. *Bulletin of mathematical biology*, 74(11):2570–2599, 2012.
- [66] Calina Copos and Alex Mogilner. A hybrid stochastic-deterministic mechanochemical model of cell polarization. Molecular Biology of the Cell, 31(15):1637–1649, 2020.
- [67] Brian A Camley, Yunsong Zhang, Yanxiang Zhao, Bo Li, Eshel Ben-Jacob, Herbert Levine, and Wouter-Jan Rappel. Polarity mechanisms such as contact inhibition of locomotion regulate persistent rotational motion of mammalian cells on micropatterns. Proceedings of the National Academy of Sciences, 111(41):14770-14775, 2014.
- [68] Hans Gruler and Richard Nuccitelli. The galvanotaxis response mechanism of keratinocytes can be modeled as a proportional controller. *Cell Biochemistry and Biophysics*, 33(1):33–51, 2000.
- [69] Xiaoting Meng, Miguel Arocena, Josef Penninger, Fred H Gage, Min Zhao, and Bing Song. PI3K mediated electrotaxis of embryonic and adult neural progenitor cells in the presence of growth factors. Experimental Neurology, 227(1):210–217, 2011.
- [70] Erik Finkelstein, Winston Chang, P-H Grace Chao, Dorota Gruber, Audrey Minden, Clark T Hung, and J Chloë Bulinski. Roles of microtubules, cell polarity and adhesion in electric-field-mediated motility of 3T3 fibroblasts. *Journal of Cell Science*, 117(8):1533-1545, 2004.
- [71] Rachael A Ream, Julie A Theriot, and George N Somero. Influences of thermal acclimation and acute temperature change on the motility of epithelial wound-healing cells (keratocytes) of tropical, temperate and antarctic fish. *Journal of Experimental Biology*, 206(24):4539–4551, 2003.
- [72] Thomas P Prescott, Kan Zhu, Min Zhao, and Ruth E Baker. Quantifying the impact of electric fields on single-cell motility. Biophysical Journal, 120:3363–3373, 2021.
- [73] Erin L Barnhart, Kun-Chun Lee, Kinneret Keren, Alex Mogilner, and Julie A Theriot. An adhesion-dependent switch between mechanisms that determine motile cell shape. *PLoS Biology*, 9(5):e1001059, 2011.
- [74] Brian A Camley, Juliane Zimmermann, Herbert Levine, and Wouter-Jan Rappel. Collective signal processing in cluster chemotaxis: Roles of adaptation, amplification, and co-attraction in collective guidance. *PLoS Computational Biology*, 12(7):e1005008, 2016.
- [75] Ankit Rohatgi. WebPlotDigitizer: Version 4.5, 2021.
- [76] Börn Meier, Alejandro Zielinski, Christoph Weber, Delphine Arcizet, Simon Youssef, Thomas Franosch, Joachim O Rädler, and Doris Heinrich. Chemotactic cell trapping in controlled alternating gradient fields. Proceedings of the National Academy of Sciences, 108(28):11417–11422, 2011.
- [77] Runchi Gao, Siwei Zhao, Xupin Jiang, Yaohui Sun, Sanjun Zhao, Jing Gao, Jane Borleis, Stacey Willard, Ming Tang, Huaqing Cai, et al. A large-scale screen reveals genes that mediate electrotaxis in dictyostelium discoideum. *Science Signaling*, 8(378):ra50-ra50, 2015.
- [78] Naoko Ogawa, Hiromasa Oku, Koichi Hashimoto, and Masatoshi Ishikawa. Microrobotic visual control of motile cells using high-speed tracking system. *IEEE Transactions on Robotics*, 21(4):704–712, 2005.

[79] Naoko Ogawa, Hiromasa Oku, Koichi Hashimoto, and Masatoshi Ishikawa. A physical model for galvanotaxis of paramecium cell. *Journal of Theoretical Biology*, 242(2):314–328, 2006.

Supplemental Information for "Self-propelled deformable particle model for keratocyte galvanotaxis"

Appendix A: Interpreting shape-velocity coupling

In our equations of motion for the velocity, we have a term $\vec{\mathbf{S}} \cdot \mathbf{v}$, which is a matrix product, i.e. its α th component is $S_{\alpha\beta}v_{\beta}$.

We can write

$$\vec{\mathbf{S}} = s \begin{pmatrix} \cos^2 \theta - \frac{1}{2} & \cos \theta \sin \theta \\ \cos \theta \sin \theta & \sin^2 \theta - \frac{1}{2} \end{pmatrix} = \frac{s}{2} \begin{pmatrix} \cos 2\theta & \sin 2\theta \\ \sin 2\theta & -\cos 2\theta \end{pmatrix}. \tag{A1}$$

The eigenvectors of $\vec{\mathbf{S}}$ are just the unit vectors parallel to the axis, $\hat{\mathbf{n}} = (\cos \theta, \sin \theta)$ and perpendicular to it, $\hat{\mathbf{n}}_{\perp} = (-\sin \theta, \cos \theta)$, with eigenvalues $\pm s/2$, respectively. If we break up the velocity into the components perpendicular to and parallel to the long axis, $\mathbf{v} = v_{\parallel}\hat{\mathbf{n}} + v_{\perp}\hat{\mathbf{n}}_{\perp}$, then

$$\begin{split} \vec{\mathbf{S}} \cdot \mathbf{v} &= \vec{\mathbf{S}} \cdot (v_{\parallel} \hat{\mathbf{n}} + v_{\perp} \hat{\mathbf{n}}_{\perp}) \\ &= \frac{s}{2} v_{\parallel} \hat{\mathbf{n}} - \frac{s}{2} v_{\perp} \hat{\mathbf{n}}_{\perp}. \end{split}$$

Thus, revisiting Eq. 1, we see that $-a\mathbf{S} \cdot \mathbf{v} = -as(v_{\parallel}\hat{\mathbf{n}} - v_{\perp}\hat{\mathbf{n}}_{\perp})/2$. When a < 0, as is true everywhere in the main paper, this term then makes the velocity component along the long axis $\hat{\mathbf{n}}$ increase while the component along the short axis decreases – this term makes the velocity align more along the long axis of the cell.

Appendix	B:	Model	calibration	and	fitting

Parameter	Value		Description	Source
v_0	10	$\mu \mathrm{m \ min^{-1}}$	characteristic keratocyte velocity	[42, 43]
γ	v_0^2	$\mu \mathrm{m}^2 \mathrm{min}^{-2}$	propulsion term	defined as v_0^2
κ	1.3068	\min^{-1}	shape relaxation rate	fit
χ	0.0720	\min^{-1}	rate of velocity aligning with polarity	fit
τ	0.0617	min	time scale of polarity aligning with velocity	fit
$ au_{ m b}$	0.0238		time scale of polarity aligning with bias	fit
ω_0	0.9758	\min^{-1}	characteristic frequency of keratocyte rotation,	fit constrained by [18]
			defined as $\omega_0 = \mu v_0^2$	
σ	0.3372	$\mu \mathrm{m \ min}^{-1.5}$	velocity rotational noise	fit
$\sigma_{ m p}$	0.7058		polarity displacement noise	fit
a	-0.1132	$\mu {\rm m}^{-1} {\rm min}^{-1}$		fit
			0 means velocity along cell's long axis increases)	
b	-0.5423	$\min \mu m^{-1}$	controls rate of shape responding to velocity ($b <$	fit
			0 means cell shape expands perpendicular to ve-	
			locity direction)	
Δt	0.001	min	time step for simulations	

TABLE I: Table of parameter values, description, and sources.

Where possible, we use well-known cell parameters for shape, size, and speed. We choose a characteristic speed of $v_0 = 10 \ \mu \text{m min}^{-1}$ [42, 43], which fixes $\gamma = v_0^2$. We note that the actual speed of the cell will depend on other parameters other than γ (see Appendix D); we have only set its rough order of magnitude by choosing v_0 .

To set the remainder of our parameters, we fit our model to the experimental results of Allen *et al.* [20], who studied cell directionality in response to an electric field being turned on (shown in Fig. 4). We extracted this data with WebPlotDigitizer [75]. The experiments show that if the cell's velocity has an angle ϕ to the x-axis, the average directionality $\langle \cos \phi \rangle$ increases to a steady state value over a time of $\sim 5-10$ minutes after the field is turned on (Fig. 4).

The parameters that needed to be calculated were $a, b, \kappa, \omega_0, \chi, \tau, \tau_b, \sigma$, and σ_p ; we reparameterized $\mu = \omega_0/v_0^2$, where ω_0 is the characteristic keratocyte rotational frequency [18]. To get our fit parameters, we picked from a broad range of plausible values (See Appendix C) using Latin hypercube sampling, and then ran a simulation to match the experiment by having no electric field when t < 15 min, then setting $\mathbf{E} = [1,0]$ when $t \ge 15$ min. To minimize the influence of initial conditions, we simulate 2 hours of trajectory as equilibration time before the t = 0 point of the trajectories shown in Fig. 4. We ran 1000 repeated simulations to construct the average directionality $\langle \cos \phi \rangle$ over time. The same procedure of equilibration and averaging was conducted for the curves in Fig. 5, but with 500 simulations. Parameter sets that led to numerical instabilities were discarded; we found these largely corresponded to cells oscillating unphysically fast. We then chose the parameters that created the best-fitting directionality curve, according to our criterion (see Eq. B2 below).

We know that in order to observe both circular motion and persistent motion, as seen experimentally, we must have our parameters close to the transition between circular and straight motion (see Section III). To ensure we are near this transition point, and to reduce the number of fit parameters, we constrained the possible fit values for b and κ using two pieces of information: 1) the rough experimental aspect ratio of keratocytes, and 2) the idea that the cells must be near the transition between circular and persistent motion. The value of the shape deformation parameter s emerges from the model; if the cell is at steady state in a straight line, it takes on the value

$$s_{\rm ss} = -\frac{b}{\kappa} \frac{\mu \gamma}{\beta + \mu}$$
, where $\beta = \frac{ab}{2\kappa}$.

Note that a, b < 0. The values κ and b that would be found if the parameters were at the transition line and at steady state are

$$\kappa_1 = -as - (\chi + \tau^{-1}), \quad \kappa_2 = \frac{-as}{\chi \tau + 1},$$

$$b_{\rm T} = -\frac{2s\mu\kappa}{2\gamma\mu + as},$$

where $s=s_{\rm ss}$ is the value of s in the steady-state with the cell crawling straight (Appendix D). κ_1 and κ_2 are derived from γ_1 and γ_2 , respectively. $b_{\rm T}$ is derived by rearranging $s_{\rm ss}$, where $\gamma=v_0^2$ (Appendices C and D). There are two equations for κ . Choosing $\kappa=\kappa_1$ sets the system to the transition line in the phase diagram if $\gamma_1<\gamma_2$, and choosing $\kappa=\kappa_2$ sets the system to the transition line if $\gamma_2<\gamma_1$. For all the plausible range of parameters shown in Table II, $\gamma_2<\gamma_1$ and so we always choose κ to be near κ_2 (Table II). In setting κ and b, we assume $s_{\rm ss}=12.5~\mu{\rm m}$, which sets the aspect ratio of the keratocyte. We know experimentally that the roughly elliptical keratocyte cells of interest that we were modeling had an radius of $R_0=14.5~\mu{\rm m}$ for an equivalent circle of the same area. We then choose the steady state value of $s=s_{\rm ss}=12.5~\mu{\rm m}$, which ensures that the aspect ratio of the cell, $(R_0+s/2)/(R_0-s/2)\approx 2.5$.

Our goal is to find the parameter set that minimized the error between simulations and experiment – but we suspect from our simulations that many of the oscillations about the steady-state value in the experimental data of Fig. 4 are from the finite sample size of 140 cells. To avoid overfitting, we have chosen not to directly minimize the error between simulation and experiment in $\langle \cos \phi \rangle$ (Fig. 4). Instead, we want our model to correctly capture the response time and steady-state directionality of the data. We fit both the simulated and experimental measurements of $\langle \cos \phi \rangle$ to a hyperbolic tangent function:

$$\langle \cos \phi \rangle = A \tanh \left(\frac{t - t_{\rm s}}{\tau_{\rm r}} \right) + B.$$
 (B1)

using MATLAB's nlinfit. As described above, the simulation curves of $\langle \cos \phi \rangle$ were constructed from averaging together 1000 simulations of the field being turned on. In this fit function, t_s is the time of the inflection point of $\tanh(\cdot)$ i.e. the time where the derivative is maximal. τ_r is the scaling factor that determines how "wide" the function is at the transition. Physically, τ_r sets the scale of the time the cell takes to respond to an electric field being turned on. The other key parameter in the fitting form Eq. B1 is the long-time value of the directionality, $SS = \lim_{t\to\infty} \langle \cos \phi \rangle = A + B$. We found the values $\tau_{\rm expt}$ and $SS_{\rm expt}$ from fitting the experimental curve to Eq. B1. We then chose, among the range of parameters, the parameters that minimize the error ϵ in steady-state value SS = A + B and response time τ_r between the experiment and theory:

$$\epsilon = \left(\frac{\tau_{\rm r} - \tau_{\rm expt}}{\tau_{\rm expt}}\right)^2 + \left(\frac{SS - SS_{\rm expt}}{SS_{\rm expt}}\right)^2.$$
 (B2)

The resulting wild-type parameters are shown in Table I.

The errors bars in Fig. 4 were calculated with the bootstrap method. 100 of the 1000 simulated cells were sampled and the mean of their response was calculated. This process was repeated for 100 samples. The standard deviation of the mean responses of the 100 samples were calculated and used as the error bars.

Appendix C: Parameter range variation

We show in Table II the ranges of parameter values used to fit in our Latin hypercube process.

Parameter	Range	Comments
κ	$[0.9, 1.1]\kappa_{1,2}$	Linearly spaced
χ	[0.01, 0.1]	Logarithmically spaced
au	[0.01, 0.1]	Logarithmically spaced
$ au_{ m b}$	$[0.01, 10]\tau$	Logarithmically spaced
ω_0	$[0.9, 1.1] \frac{\pi}{2} \text{rad}$	This constraint is both from the rough timescale of $\omega_0 \sim 1 \text{ deg/s}$
	3	[18] and earlier fits, which pointed at this being the plausible
		range.
σ	$[0.01, 0.1]\sqrt{v_0^2\omega_0}$	Linearly spaced
$\sigma_{ m p}$	$[0.01, 0.1]\sqrt{v_0^2\omega_0}$	Linearly spaced
a	-[0.1, 1]	Logarithmically spaced; a is required to be negative so that the
		velocity along the long axis of the cell increases, leading to the
		turning instability (Appendix A).
b	$[0.9, 1.1]b_{\mathrm{T}}$	Linearly spaced; b is constrained to be near the value given by
		the transition condition (Appendix B). b is also required to be
		negative so that $ab > 0$, which is necessary for the instability to
		occur [24].

TABLE II: Table showing range over which parameters were varied in the fit.

Appendix D: Linear stability analysis

We start by finding the stationary solutions of the deterministic portions of Eqs. 2-4, which are a first step to finding linear stability but are also interesting in their own right. First, let us define $\mathbf{v} = v(\cos\phi, \sin\phi)$, where $v_1 = v\cos\phi$ and $v_2 = v\sin\phi$ are the first and second components, respectively. Earlier, we defined $\hat{\mathbf{n}} = (\cos\theta, \sin\theta)$ and $\hat{\mathbf{p}} = (\cos\phi_p, \sin\phi_p)$, meaning that n_1, n_2, p_1, p_2 can be defined the same way v_1 and v_2 were defined. Knowing the components of $\hat{\mathbf{n}}$ allow us to list the components of $\hat{\mathbf{S}}$ using Eq. 1. Second, it will serve us to rewrite the deterministic portions of Eqs. 2 and 3 component-wise:

$$\frac{\mathrm{d}v_{\alpha}}{\mathrm{d}t} = \mu(\gamma - v^2)v_{\alpha} - aS_{\alpha\beta}v_{\beta} - \frac{\chi}{v}(v_{\alpha}v_{\beta} - v^2\delta_{\alpha\beta})p_{\beta},$$

$$\frac{\mathrm{d}S_{\alpha\beta}}{\mathrm{d}t} = -\kappa S_{\alpha\beta} + b\left(v_{\alpha}v_{\beta} - \frac{1}{2}v^{2}\delta_{\alpha\beta}\right).$$

where we have implicitly assumed Einstein summation. After making the appropriate substitutions for the components of \mathbf{v} , $\hat{\mathbf{p}}$, and $\hat{\mathbf{n}}$, one can derive equations for the velocity magnitude, v, the angle of the velocity, ϕ , the shape change s, and the angle of the major axis θ i.e. Eqs. D1-D4. To derive Eq. D1, one must calculate $\hat{\mathbf{v}} \cdot \partial_t \mathbf{v} = (\cos \phi)\partial_t v_1 + (\sin \phi)\partial_t v_2$. To derive D2, one must calculate $\hat{\mathbf{v}}_{\perp} \cdot \partial_t \mathbf{v} = (-\sin \phi)\partial_t v_1 + (\cos \phi)\partial_t v_2$. To derive Eqs. D3 and D4, one must calculate $(\cos 2\theta)\partial_t S_{11} + (\sin 2\theta)\partial_t S_{12}$ and $(-\sin 2\theta)\partial_t S_{11} + (\cos 2\theta)\partial_t S_{12}$, respectively. These calculations yield the following equations:

$$\frac{\mathrm{d}v}{\mathrm{d}t} = \mu(\gamma - v^2)v - \frac{asv}{2}\cos 2(\theta - \phi),\tag{D1}$$

$$\frac{d\phi}{dt} = -\frac{as}{2}\sin 2(\theta - \phi) - \chi \sin (\phi - \phi_p), \tag{D2}$$

$$\frac{\mathrm{d}s}{\mathrm{d}t} = -\kappa s + v^2 b \cos 2(\theta - \phi),\tag{D3}$$

$$\frac{\mathrm{d}\theta}{\mathrm{d}t} = -\frac{v^2 b}{2s} \sin 2(\theta - \phi). \tag{D4}$$

Following [24], assuming that we have a steady state with the cell moving in the $+\hat{\mathbf{x}}$ -direction, i.e. $\phi=0$, and that ab>0, the steady state solutions for the velocity magnitude, v, and the shape deformation, s, can be calculated by setting Eqs. D1-D4 equal to 0 and solving. When b<0, the steady state occurs when $\theta=\pi/2$ and

$$s_{\rm ss} = -rac{b}{\kappa}v_{
m ss}^2, \quad v_{
m ss}^2 = \murac{\gamma}{\beta+\mu}, \ {
m where} \ eta = rac{ab}{2\kappa}.$$

These results so far are identical to the results of Ohta and Ohkuma [24] except that we have introduced the scale μ to help make the units of the problem more explicit. At the steady state, $\phi = \phi_p$, which removes the polarity's influence in Eq. D2; thus the polarity equation does not affect the steady-state values of s or θ .

Next, for linear stability analysis we can first consider the deterministic portion of Eq. 4 without the influence of an electric field. In that case, Eq. 4 simplifies to

$$\frac{\mathrm{d}\phi_{\mathrm{p}}}{\mathrm{d}t} = -\frac{1}{\tau}\arcsin\left(\hat{\mathbf{v}}\times\hat{\mathbf{p}}\right) = \frac{\phi - \phi_{\mathrm{p}}}{\tau}.\tag{D5}$$

where we have assumed that $|\phi - \phi_p|$ is small enough that $\arcsin(\sin(\phi_p - \phi)) = \phi_p - \phi$, which will be true in our linear stability analysis below. Then, we can define two new variables, $\psi = \theta - \phi$ and $\epsilon = \phi - \phi_p$, constructing two equations for our analysis from Eqs. D1-D5:

$$\frac{\mathrm{d}\epsilon}{\mathrm{d}t} = -\frac{as}{2}\sin 2\psi - \chi\sin\epsilon - \frac{\epsilon}{\tau} \equiv f(\epsilon, \psi),\tag{D6}$$

$$\frac{\mathrm{d}\psi}{\mathrm{d}t} = -\frac{1}{2}\left(-as + \frac{bv^2}{s}\right)\sin 2\psi + \chi\sin\epsilon \equiv g(\epsilon, \psi). \tag{D7}$$

Next, we have to linearize f and g with respect to ϵ and ψ to first order. We evaluate the derivatives of f and g at $\epsilon^* = 0$ and $\psi^* = \pi/2$ (i.e. at a steady state where velocity and polarity are pointed in the same direction, but the long axis of the cell is perpendicular to this, appropriate since b < 0 for our model), giving us:

$$\frac{\mathrm{d}}{\mathrm{d}t} \begin{pmatrix} \epsilon \\ \psi \end{pmatrix} \approx \mathbf{A} \begin{pmatrix} \epsilon \\ \psi \end{pmatrix},\tag{D8}$$

where the Jacobian matrix

$$\mathbf{A} = \begin{pmatrix} \frac{\partial f}{\partial \epsilon} & \frac{\partial f}{\partial \psi} \\ \frac{\partial g}{\partial \epsilon} & \frac{\partial g}{\partial \psi} \end{pmatrix} = \begin{pmatrix} -\chi - \tau^{-1} & as \\ & & \\ \chi & -as + \frac{bv^2}{s} \end{pmatrix}.$$

Here, $s = s_{ss}$ and $v = v_{ss}$. For the solutions of our system of linearized equations to be stable, the eigenvalues of \mathbf{A} must both have negative real parts, which requires $\text{Tr}(\mathbf{A}) < 0$ and $\det(\mathbf{A}) > 0$. We can derive Eqs. 5 and 6 by solving for the γ values that set $\text{Tr}(\mathbf{A}) = 0$ and $\det(\mathbf{A}) = 0$.

The linear stability results of our model in the absence of a field reduces to that of Ohta & Ohkuma [24] in the limit where \mathbf{v} is no longer aligned with $\hat{\mathbf{p}}$ ($\chi \to 0$), but $\hat{\mathbf{p}}$ is perfectly aligned with \mathbf{v} ($\tau^{-1} \to \infty$). In this case $\gamma_1 \to \infty$ while $\gamma_2 \to \gamma_c = \frac{\kappa^2}{ab} + \frac{\kappa}{2\mu}$. As we noted above, $\mu = 1$ is chosen implicitly in [24].

We also conducted linear stability analysis with the electric field present in the deterministic portion of Eq. 4, which takes the form

$$\frac{\mathrm{d}\phi_{\mathrm{p}}}{\mathrm{d}t} = \frac{\phi - \phi_{\mathrm{p}}}{\tau} + \frac{\phi_{\mathrm{E}} - \phi_{\mathrm{p}}}{\tau_{\mathrm{b}}} = \frac{\phi - \phi_{\mathrm{p}}}{\tau} - \frac{\phi_{\mathrm{p}}}{\tau_{\mathrm{b}}}.\tag{D9}$$

 $\phi_{\rm E}=0$ since ${\bf E}=[1,0]$. To do stability analysis, we need three equations for ϵ , ψ , and $\phi_{\rm p}$, as now the angle between the polarity and the electric field is important. $f(\epsilon,\psi,\phi_{\rm p})$ gains an extra term, $+\phi_{\rm p}/\tau_{\rm b}$, while $g(\epsilon,\psi,\phi_{\rm p})$ remains unchanged and we define $\partial_t \phi_{\rm p} \equiv h(\epsilon,\psi,\phi_{\rm p})$. The resulting Jacobian matrix is

$$\mathbf{A} = \begin{pmatrix} \frac{\partial f}{\partial \epsilon} & \frac{\partial f}{\partial \psi} & \frac{\partial f}{\partial \phi_{p}} \\ \frac{\partial g}{\partial \epsilon} & \frac{\partial g}{\partial \psi} & \frac{\partial g}{\partial \phi_{p}} \\ \frac{\partial h}{\partial \epsilon} & \frac{\partial h}{\partial \psi} & \frac{\partial h}{\partial \phi_{p}} \end{pmatrix} = \begin{pmatrix} -\chi - \tau^{-1} & as & \tau_{b}^{-1} \\ \chi & -as + \frac{bv^{2}}{s} & 0 \\ \tau^{-1} & 0 & -\tau_{b}^{-1} \end{pmatrix}.$$
(D10)

where the derivatives are evaluated at the appropriate steady-state values of ϵ , ψ , and $\phi_{\rm p}$.

For the solutions to be stable, all three eigenvalues of **A** must have a negative real part. The analytical form for these conditions are cumbersome; we show stability diagrams determined by numerically finding the eigenvalues of **A** in Fig. 3B.

Appendix E: Phase diagram for cells that move along their long axis

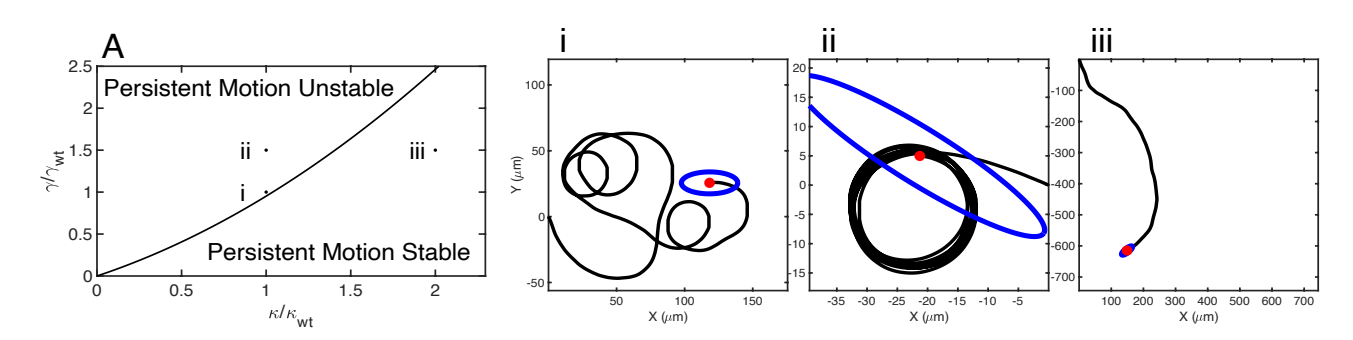


FIG. S1: (A): Linear stability phase diagram in $\gamma - \kappa$ plane in the absence of electric field for a, b > 0. a and b have the same values as Table I, but with signs flipped. Example trajectories for points i-iii are shown. (i): shows a 2.5-hour trajectory at the "wild-type" (WT) values, $(\gamma = \gamma_{\rm wt}, \ \kappa = \kappa_{\rm wt})$. (ii): 1-hour trajectory when cell speed is increased slightly, resulting in persistent circular motion, $(\gamma = 1.5\gamma_{\rm wt}, \ \kappa = \kappa_{\rm wt})$. (iii): 1.5-hour trajectory with greatly increased shape relaxation rate κ shows persistent random walk, $(\gamma = 1.5\gamma_{\rm wt}, \ \kappa = 2\kappa_{\rm wt})$.

Throughout this manuscript, we have fixed a, b < 0 to best emulate keratocyte behavior, which includes both persistent motion with the cell velocity perpendicular to the long axis and circular motion. If we fix a, b > 0, this might be more appropriate for other eukaryotic cell types such as $Dictyostelium\ discoideum\ and\ Paramecium\ which undergo galvanotaxis parallel to their long axis [76–79]. When <math>a > 0$, velocities along the cell's major axis will decrease, and velocities along the cell's minor axis will increase, leading the velocity to align to $\pm \hat{\mathbf{n}}_{\perp}$ (Appendix A). When b > 0, cells contract their shape perpendicular to the direction of the velocity and expand parallel to the velocity.

Additional stability analysis reveals the regime our model is effective for emulating other cell behavior. Starting with Eqs. 2-4, the steady state of a cell moving in the $+\hat{\mathbf{x}}$ -direction occurs when $\theta=0$, giving us $v_{\rm ss}^2=\mu\gamma/(\beta+\mu)$ and $s_{\rm ss}=+bv_{\rm ss}^2/\kappa$. We can follow a similar procedure and define $\psi=\theta-\phi$ and $\epsilon=\phi-\phi_{\rm p}$ and rewrite Eqs. 2-4 as Eqs. D6 and D7. Evaluating the derivatives at $\epsilon^*=0$ and $\psi^*=0$ produces the Jacobian matrix

$$\mathbf{A} = \begin{pmatrix} -\chi - \tau^{-1} & -as \\ & & \\ \chi & as - \frac{bv^2}{s} \end{pmatrix}.$$

Linear stability analysis of this Jacobian reveals two new transition lines:

$$\gamma_3 = \frac{\kappa^2}{ab} + \left(\frac{1}{2\mu} - \frac{\chi + \tau^{-1}}{ab}\right)\kappa - \frac{\chi + \tau^{-1}}{2\mu},\tag{E1}$$

$$\gamma_4 = \frac{1 - \chi \tau}{ab} \kappa^2 + \frac{1 - \chi \tau}{2\mu} \kappa. \tag{E2}$$

Unlike in the main text, stability occurs when $\gamma_3 < \gamma < \gamma_4$. This requirement simplifies to $\gamma < \gamma_4$ since $\gamma > 0$ and γ_3 is always negative for the range of parameters investigated here (for example, $\kappa \gg 1000\kappa_{\rm wt}$ is necessary to have $\gamma_3 > 0$). The linear stability results for a, b > 0 also reduces to [24] when $\mu = 1$ in the limit where \mathbf{v} is no longer aligned

with
$$\hat{\mathbf{p}}$$
 ($\chi \to 0$), but $\hat{\mathbf{p}}$ is perfectly aligned with \mathbf{v} ($\tau^{-1} \to \infty$). In this case $\gamma_3 \to -\infty$ while $\gamma_4 \to \gamma_c = \frac{\kappa^2}{ab} + \frac{\kappa}{2\mu}$.

We observe the same type of behaviors above and below the transition line (Fig. S1) like we see in Fig. 3 of the main text. Note that the phase diagram of Fig. S1 looks indistinguishable from the phase diagram in Fig. 3A, even though $\gamma_2 \neq \gamma_4$, for two reasons: first, the product ab remains the same since a and b have the same absolute value but opposite signs from Table I; second, the coefficients for κ^2 and κ are virtually identical, since $\chi \tau \approx 0.0044 \rightarrow 1 \pm \chi \tau \approx 1$.

Appendix F: Probability density plots

In Fig. 6, we showed the effect of a rapidly switching fields in terms of the probability density of angles of the cell velocity. In these simulations, the field was switched between the $+\hat{\mathbf{x}}$ - and $+\hat{\mathbf{y}}$ -directions with "exposure times" $t_{\rm ET}$ ranging from every 2.5 minutes to 2.5 hours. The simulation was run for a total of $t_{\rm max}=100$ hours. To measure the cell response, we calculated the angle between the average cell velocity in a given time window and the reference angle $\phi_{\rm r}=\pi/4$, which is the average direction of the changing field. Algorithm:

- 1. Simulate the cell and find $\mathbf{v}(t)$ for a time t_{ET} , keeping the field constant.
- 2. Compute the average velocity over this time, \bar{v}
- 3. Find the angle between \bar{v} and $\phi_{\rm r}$ and store: $\Delta \phi = \phi_{\rm cell} \phi_{\rm r}$, where $\phi_{\rm cell} = \arctan(\bar{v}_2/\bar{v}_1)$
- 4. Switch the field direction and then repeat steps 1-3 until total time $t_{\rm max}$.
- 5. Plot probability density of angles.

Appendix G: Supplementary figures and movie captions

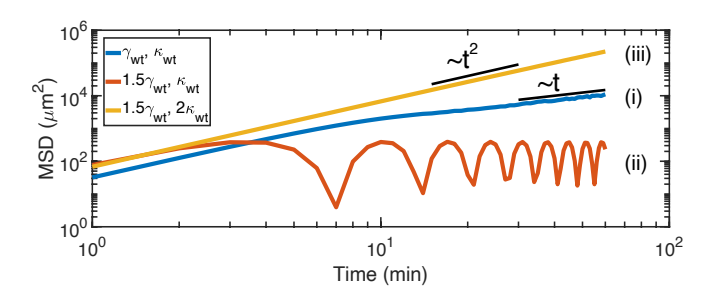


FIG. S2: Mean squared displacement for cases i, i, and iii of Fig. 3. Each MSD is computed from a a single long trajectory of total length of 200 simulation hours.

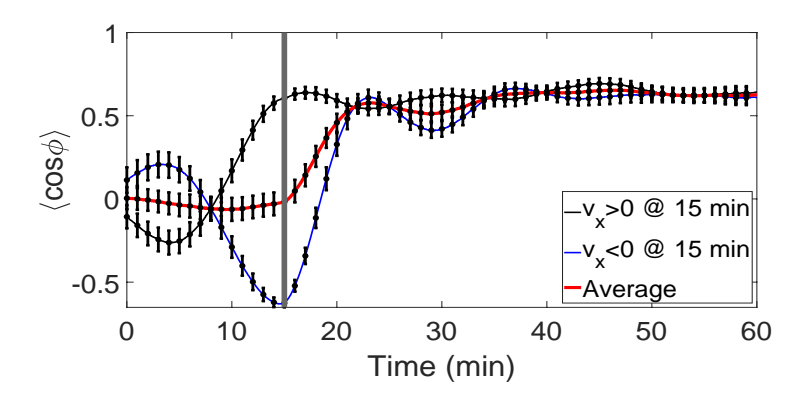


FIG. S3: Cell response to field depending on whether the cell was at t = 15 minutes facing away (black) or facing towards (blue) the field direction, juxtaposed with the overall average from Fig. 4 (red). These are all constructed from the same set of 1000 cells simulated in Fig. 4, but averaged only over the relevant trajectories.

In all movies, the magnitude |v| shows the magnitude of the velocity in units of μ m/min. The red arrow in the left panel shows the presence and direction of an electric field. Parameters not stated explicitly are given by the default values in Table I.

Movie S1: Trajectory of wild-type cell without any field.

Movie S2: Trajectory of cell at $1.5\gamma_{\rm wt}$ without any field.

Movie S3: Trajectory of cell at $1.5\gamma_{\rm wt}$ and $2\kappa_{\rm wt}$ without any field.

Movie S4: Trajectory of cell at $8\chi_{\rm wt}$ with no noise. Field turns on after first 120 minutes.

Movie S5: Trajectory of wild-type cell with slowly switching electric field ($t_{\rm ET}=2.5$ hours).

Movie S6: Trajectory of wild-type cell with rapidly switching electric field ($t_{\text{ET}} = 5$ minutes).

Movie S7: Trajectory of cell at $5\gamma_{\text{wt}}$ with switching electric field ($t_{\text{ET}} = 80$ minutes). Cells rotate while showing drift perpendicular to field direction.

Movie S8: Trajectory of cell at $0.25\chi_{\rm wt}$ with switching electric field ($t_{\rm ET}=80$ minutes). At these parameters, the polarity follows the field reliably but the cell direction does not.

Movie S9: Trajectory of wild-type cell showing an "oversteering" response when the field turns on after first 120 minutes.